Inaugural-Dissertation

zur
Erlangung der Doktorwürde
der
Naturwissenschaftlich-Mathematischen
Gesamtfakultät
der
Ruprecht-Karls-Universität
Heidelberg

vorgelegt von

Diplom-Informatiker Jochen Schmähling
aus Bad Kissingen

Tag der mündlichen Prüfung: 28.6.2006

Statistical characterization of technical surface microstructure

Gutachter: Prof. Dr. Fred A. Hamprecht
Prof. Dr. Peter Bastian

Abstract

In the development and production of industrial parts, both the macroscopic shape and the microstructure of the parts surface on a μm-scale strongly influence the parts properties. For instance, a surface in frictional contact should be structured in a way to reduce the expected wear by optimizing its lubrication properties. A gasket surface must not be too rough to prevent leakage, etc.

The measurement of surface roughness started a few decades ago with the advent of tactile profilometers. These drag a stylus along a line over the surface and record the vertical deflection of the stylus as it moves over the surface, thus recording the height of the surface at the sampling points. Modern measurement techniques make it possible to acquire a complete three-dimensional height map of the surfaces. Obviously, the techniques for analysing two-dimensional profiles are not adequate for the analysis of three-dimensional height maps.

Although many propositions for 3D-analysis have been made, these often lack a sound theoretical background. Hence, their understanding is limited and only a few are used regularly, resulting in an inadequate surface description.

A simple but powerful approach is to use the Minkowski functionals of the excursion sets of the data to charactarize the surface structure. These functionals can be interpreted in different ways depending on the model for the surface. Two models seem especially suited for technical surfaces: Random fields for surfaces with no obvious structure, e.g. shot-blasted surfaces and Boolean grain models for surfaces consisting of smaller structuring elements, e.g. sintered materials.

In this thesis, a complete framework for the analysis of three-dimensional surface data using the Minkowski functionals is developed. This novel approach allows for a stepwise data reduction: A complex data set is first reduced to three characterizing functions, from which further parameters can be derived.

Due to a novel fast and accurate estimator for the characterizing functions, this technique is also suitable for time-critical tasks like the application in production automation.

Zusammenfassung

In der Entwicklung und Produktion industrieller Bauteile werden die Bauteileigenschaften sowohl durch die makroskopische Form als auch durch die Mikrostruktur der Oberfläche im μm-Bereich erheblich beeinflusst. Beispielsweise sollten Oberflächen, die in Reibkontakt stehen, so strukturiert werden, dass der erwartete Verschleiß durch Optimierung der Schmiereigenschaften minimiert wird. Oberflächen von Dichtungen sollten nicht zu rau sein um ein Leckwerden zu verhindern etc.

Die Untersuchung der Mikrostruktur von Oberflächen beginnt historisch mit dem Einsatz von Tastschnitt-Messgeräten, die die Oberfläche mit einem Taststift abfahren und entlang der Verfahrstrecke ein zweidimensionales Höhenprofil aufzeichnen. Der Einsatz moderner optischer Messtechnik ermöglicht nun auch die dreidimensionale Vermessung einer Oberfläche. Es ist offensichtlich, dass sich die Analysetechniken für zweidimensionale Profilschnitte nur bedingt für die Analyse dreidimensionaler Höhenkarten eignen.

Obwohl viele Vorschläge für eine 3D-Analyse erarbeitet wurden, fehlt diesen häufig eine fundierte theoretische Grundlage. Deshalb sind diese Techniken nur in begrenztem Maße mathematisch analysierbar. Nur wenige werden in der Praxis regelmäßig eingesetzt, was eine unzureichende Beschreibung der Oberflächenstrukturen zur Folge hat.

Ein einfacher aber mächtiger Ansatz ist die Verwendung von Minkowskifunktionalen von Exkursionsmengen der Daten zur Charakterisierung der Oberflächenstruktur. Diese Funktionale können abhängig von einem Oberflächenmodell unterschiedlich interpretiert werden. Zwei Modelle erscheinen für technische Oberflächen besonders geeignet: Zufallsfelder eignen sich für Oberflächen ohne ausgeprägte Struktur, zum Beispiel gestrahlte Oberflächen; Boolesche Kornmodelle eignen sich für Oberflächen, die, wie beispielsweise Sintermaterialien, aus kleineren Strukturelementen zusammengesetzt sind.

In dieser Arbeit wird ein System zur Analyse dreidimensionaler Oberflächendaten durch Minkowskifunktionale entwickelt. Dieser neuartige Ansatz erlaubt eine schrittweise Reduktion der in den Messdaten enthaltenen Information: Ein umfangreicher Datensatz wird zunächst in drei charakterisierenden Funktionen zusammengefasst, aus denen weitere Kenngrößen abgeleitet werden können.

Durch eine neue Berechnungsmethode, die eine sehr effiziente und genaue Schätzung der Minkowskifunktionale aus Messdaten erlaubt, lassen sich die charakterisierenden Funktionen auch für zeitkritische Aufgaben wie eine automatisierte Prozesskontrolle einsetzen.

Contents

Preface

This thesis has emerged from my work in the Automatic Optical Inspection Group in the research and development department of Robert Bosch GmbH, Stuttgart.

First of all, I would like to thank my doctoral advisor, Prof. Fred Hamprecht from the Interdisciplinary Institute of Scientific Computing (IWR), University of Heidelberg, who initially triggered this thesis. Throughout my stay with Bosch, his continuous encouragement and extraordinary commitment have been key factors for the final success of this project.

I would like to thank Walter Happold from Robert Bosch GmbH for offering me the possibility to prepare my doctoral thesis in such a challenging and proliferous environment. Thanks also go to Ralf Zink, my tutor at Bosch, for the fruitful discussions and for the insight in the physical background of optical measurement systems. Furthermore I owe gratitude to Dominik Hoffmann, who laid the basis for the work tackled in chapter 6 of this thesis, for his help and encouragement.

I am indebted to my colleagues at Bosch and to the fellow doctoral students at Bosch, especially Michael, Thomas, Marco, Stefan, Linus, Mark, Thomas and Andreas (in chronological order), for creating an inspiring and pleasant working atmosphere.

Last but not least, thanks go to the Multidimensional Image Processing Group at the IWR, for their support and sympathy.

Stuttgart, April 2006

Kunst

Ein Mensch malt, von Begeistrung wild,
drei Jahre lang an einem Bild.
Dann legt er stolz den Pinsel hin
und sagt: “Da steckt viel Arbeit drin.”
Doch damit war’s auch leider aus:
Die Arbeit kam nicht mehr heraus.

(Eugen Roth)

1. Introduction

In the development and production of industrial parts, both the macroscopic shape and the microstructure of the surface strongly influence its properties. The decreasing dimension of parts – micromechanic devices are already state of the art – and the growing stress that materials should be able to cope with also highlight their surface microstructure. As a consequence, the measurement and inspection of surface microstructure has found a long-time and still growing interest from both researchers and engineers.

Statistical surface microstructure analysis Surface microstructure analysis is used for two major purposes. The first task is *specification* and *inspection*, especially for quality assurance in industrial applications. Here, the task is to specify the surface to be manufactured and afterwards check whether a surface has been produced according to the manufacturing specifications. The second task is *functional correlation*, where the surface microstructure is correlated with the functional behavior of the part. Such a correlation is fundamental for the understanding of existing and the development of novel surface finishing methods.

Surfaces in frictional contact have to be structured such that the expected wear is as small as possible; the surface structure has to guarantee an optimal lubrication. For steel sheets, the surface microstructure has an influence on the machining properties in recasting; also the quality of a subsequent varnishing can be determined. Finally, there are materials where the surface structure is crucial for the part's functionality. One example are filter materials, where the surface area is correlated with the filtration effect. These are just a few examples where the surface microstructure is important. The number of applications is growing steadily; the fine-tuning of materials will be even more important in the future.

Along with the diversity of applications also many types of surface microstructure exist. The microstructure can either be a property inherent to the material or be produced by a separate machining step. There are surfaces with deterministically placed microstructure; one example is the drilling of tiny craters in a smooth surface using a laser, which can improve the lubrication properties. Other materials consist of tiny metal grains fused in a thermal process; the surface has a random structure, but the grains are still apparent as structuring elements. Completely random structures instead result from machining processes like etching or grinding.

The aim of statistical surface microstructure characterization is to calculate features from surface measurements. These features should contain the information relevant for a given application and exclude irrelevant information like measurement noise. Feature calculation usually performs some information reduction. Often a complex data set is reduced to a scalar valued feature, usually referred to in literature as *surface microstructure parameter*[1] or simply *parameter*, which can be compared to predefined bounds in a specification and inspection task or compared to some physical property to find a functional correlation.

Industrial practice in surface microstructure analysis Historically, the investigation of surface microstructure started a few decades ago with the advent of so-called profilometers, which are still the standard tool used in industrial applications. Tactile profilometers record the vertical deflection of a stylus that is moved along a line over the surface. In their long-termed development, profilometers have reached a high precision. Still, as the stylus has permanent contact with the surface, it is easily soiled or damaged, and the speed of the measurement is limited. Although it is theoretically possible to acquire a full 3D height map by recording many parallel profile sections, this is in general not feasible due to time limitations. Moreover, parallel profile sections might not match exactly due to artifacts, and measuring the same surface with differing recording directions could show significant discrepancies [41].

The availability of profile measurement systems and the resulting limited data sets also entailed the evaluation methods used for surface microstructure characterization. Up to now the statistical methods mainly used in practice for surface analysis are based on the evaluation of one – or for the sake of statistical robustness also several – profile sections of the surface. The measurement data is available as height values over a scalar valued coordinate. Such a height profile is usually referred to as 2D data[2]. In contrast, 3D parameters are defined for measurements of all height values over a plain.

The limitations of 2D analysis methods are obvious; first of all, a 3D mea-

[1] The term *surface roughness parameter* used in the major part of the references might be misleading as it suggests surfaces to be rough in the sense of not showing an observable structure.

[2] There is a nomenclature conflict between signal/image processing literature and surface microstructure analysis literature. In the former, vector-valued data like time series are called one-dimensional and images are called two-dimensional, while in the latter vector-valued data is referred to as two-dimensional and images as three-dimensional data. In this work, the nomenclature of surface microstructure analysis literature will be used, though the mathematically correct description for profile sections respective height maps would be "one(two)-dimensional manifolds embedded in $\mathbb{R}^2(\mathbb{R}^3)$".

surement usually contains much more data, and therefore allows for a statistically more robust analysis. Second, a lot of surface microstructures are directional, and the recording direction of a profile measurement can have a large influence on the outcome. In the case of a plateau honed surface, which consists of a plateau crossed by parallel troughs in two major directions, the measurement along a trough will certainly differ from a measurement vertical to the trough. Third, and most important, surface microstructure is a spatial phenomenon, and although statistics of a profile section might reveal the major information content of the surface in some special cases, and analysis techniques applicable to a broad range of surfaces will require complete 3D measurements.

More recently, 3D-measuring instruments such as interferometry or fringe projection have become available for surface microstructure inspection, and their development is still ongoing. These can acquire an entire 3D height map at once and store it as a 2D image. The optical instruments are fast and contactless and are thus well suited for the application in an industrial environment. The new 3D measurement devices in combination with fast computers offer new possibilities: As 3D height maps are basically 2D images, virtually all methods developed in image processing are also applicable to the analysis of surface microstructure[3]. Techniques include but are not limited to digital filters [13], spectral analysis [45], texture analysis [58] and topographic feature extraction [79], see chapter 2.

Standardization of surface microstructure parameters An important aspect of surface microstructure characterization is standardization. Any characteristic to appear in a technical drawing has to be part of a published standard – otherwise, it cannot be guaranteed that the outcome of a surface finishing process matches the intention of the designer. As of now, a standard for surface texture exists only for profile data [31, 30]; for areal measurements, a standard is in preparation [29].

A method to be standardized requires an unambiguous description, and preferably a simple algorithmic implementation. Moreover, a widespread use can only be expected if the characteristic is easy to understand. Abstract characteristics might make sense from the mathematician's point of view, but may ask too much even from of an experienced user.

Finally, for a measurement system to be accepted, it has to be calibrated with reference to a hardware measurement standard. For complicated characteristics, it might be difficult to produce a standard which incorporates

[3] Due to the close link between areal surface data analysis and image analysis, some nomenclature of image processing such as the notation of *pixel* for a measured amplitude at a lattice point will be used throughout this thesis.

the characteristic such that a measurement system can be calibrated. This problem reveals the dilemma with many developed characterization techniques: They might be adequate for the *description* of surfaces, but not for their *specification*.

Many image processing techniques adopted for technical surface characterization are susceptible to the mentioned problem: they are purely heuristic and difficult to implement, and their complexity hampers a standardization. Despite the longterm experience with 2D analysis, none but the simplest 2D parameters have found widespread application, and hence it is doubtful if the image processing techniques will be accepted in industry.

Aim and scope of this thesis The scope of this thesis is the development of methods for the characterization of technical surface measurement data. The focus is not so much on the derivation of single parameters but more on providing methods which allow for a derivation of further parameters. The proposed analysis techniques have a strong mathematical background and are amenable to a theoretical investigation.

An important aspect is the suitability of the proposed methods for industrial applications. Characterization results should be easily interpretable, efficient to calculate and statistically robust.

Moreover, algorithms should ideally work without any control parameters. Every necessary parameterization complicates the application, as the success strongly depends on the values chosen and therefore on the expertise of the user.

This work is concentrated mainly on data analysis aspects of surface microstructure characterization. The experiments performed to show the usefulness of the proposed techniques do not yet include results which show the correlation between the analyzed data and functionality of the surface.

Although profile measurements are of great importance in practice, current research focuses on the characterization of areal measurements. Thus, all of the methods proposed in the following chapters have been developed to work with areal data.

A Guide to this thesis In chapter 2, the state of the art of surface data characterization techniques will be reviewed. This chapter also contains some novel ideas for a systematics of methods.
Chapter 3 will lay the basis for a new surface characterization framework. Starting from a well established analysis tool, the Abbott-Firestone curve, new characteristics are developed that contain also spatial information. The introduction of surface models allows for the engineering of surface structures with specific characteristics.

Chapter 4 covers various aspects of the application in practice; furthermore, an outlook on extensions of the methods described in chapter 3 is given.
Chapter 5 shows how the proposed methods work in practice, and empirical evidence for their usefulness is given.
The thesis is concluded with a proposal for a roughness characteristic working on areal measurement data (chapter 6).

Chapters 2 and 3 summarize the state of the art and results treated in the literature. Chapters 4-6 cover topics which, to the author's knowledge, have not been addressed before in the presented way. Most important are the application of the Minkowski functionals to surface data in chapter 5, the development of a fast and accurate estimator for the Minkowski functionals in section 4.1.2 and the link of the Minkowski functionals to existing surface microstructure parameters in section 4.1.3.

2. A taxonomy of surface microstructure characterization methods

This chapter gives an overview over existing surface microstructure analysis techniques. The basic content is a review of the state of the art in areal surface texture description, but the presented taxonomy also contains some new ideas on how to classify characterization methods. The objective of this taxonomy is to help the user decide which method is suitable to describe a given data set.

When developing a taxonomy of surface microstructure parameters, it is useful to have a look at the texture analysis techniques used in image processing. Texture analysis is very similar to surface microstructure analysis, as the data under investigation and the tasks are almost identical: both try to extract characteristics which can distinguish between different realizations of data sampled on a rectangular lattice. The difference is that texture analysis features usually do not require a physical interpretation of the calculated characteristics. A taxonomy of texture parameters has been proposed in [92], and a similar system can be adopted for surface microstructure parameters.

In [92], texture analysis parameters are categorized as statistical methods, geometrical methods, filter techniques and model-based methods. Most of the methods used in surface microstructure analysis can be uniquely assigned to one of these groups (Table 2.1). The model-based approaches do not form a separate group, but are a subgroup of the others.

From the data processing point of view, all surfaces can be roughly divided into two groups[1]: The first group are stochastic surfaces, which have a random texture without observable repeated structures. The second group of surfaces has clearly defined features like ridges, craters etc. This second group can be further divided into surfaces with randomly positioned structures and those with regularly arranged structures. Obviously, this distinction is not sharp, and many surfaces contain features from both groups. For example, a surface might look stochastic at one scale but reveal geometric structures at another scale.

Nevertheless, the distinction into stochastic and geometric surfaces can give a hint which characterization techniques are adequate for a given surface at a given scale (fig. 2.1). Roughly speaking, statistical methods are

[1] In contrast, a division can also be made from the manufacturing process point of view, as proposed in [21, 85].

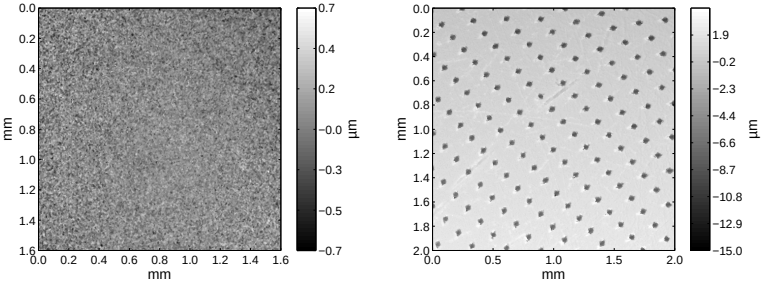

Figure 2.1.: Examples of a stochastic and a geometric surface.

appropriate for stochastic surfaces, while geometrical methods will perform best on surfaces with more or less deterministic structures. Filter techniques are appropriate for tasks which do not require a detailed description at one scale, but simple descriptions for many different scales. For example, the energy of the dominant scale could be used as a simple shape descriptor.

In the following, the different categories of characterization techniques are described in detail.

2.1. Statistical methods

Statistical methods describe the joint distribution of the measurements' height values.

Most of the profile characterization parameters defined in the standard ISO 4287 ([31], the so-called R parameter set) can be regarded as statistical, and also the major part of the S parameter set [29] designed for areal characterization belongs to the statistical methods group (table 2.1). These parameters are usually divided into amplitude, spacing, hybrid and functional parameters [9, 84]. This distinction is useful from the practitioners point of view, but is not completely satisfactory from the statistician's point of view: The so-called "amplitude" parameters are statistics over single height values, and so are the "functional" parameters. The "spacing" parameters are based on the autocorrelation function and therefore not independent of the "amplitude" parameters: As an example, consider an arbitrarily shaped autocorrelation function. Adding white uncorrelated noise to the surface will not change the spacing of its structures; nevertheless, the noise changes the autocorrelation function's amplitude in zero, and thus the width of the

Method/Parameter		Class			
		Statistical	Geometric	Filter	Model-based
S_a, S_q, S_{sk}, S_{ku}	Amplitude parameters[a]	✓			✓
S_z			✓		
S_{ds}	Spatial parameters[b]		✓		
S_{td}, S_{tdr}, S_{al}		✓			
$S_{\Delta q}$, S_{dr}	Hybrid parameters[c]	✓			
S_{sc}		✓			
S_{bi}, S_{ci}, S_{vi}	Functional parameters[d]	✓			
Level set Methods		✓	∼		✓
Co-occurrence matrices		✓			
Feature based (Motif methods)			✓		
Morph. Filters / Envelopes				✓	
Linear Systems theory				✓	
Wavelets			∼	✓	✓
Fractal methods					✓

Table 2.1.: A list of the most important methods in surface microstructure characterization. A check mark identifies a method as belonging to one of the categories; a tilde expresses that a method is comparable to the other methods in the category for a limited range of surfaces.

[a] So-called amplitude parameters [84]. S_a is the arithmetic mean deviation, S_q, S_{sk} and S_{ku} the moments 2-4 of the estimated marginal distribution. S_z is defined as the mean difference between the five highest peaks and five lowest pits of the surface.

[b] Spatial parameters, ibid. S_{ds} is the density of summits, S_{al} the fastest decay autocorrelation length, S_{tdr} the texture aspect ratio and S_{td} the texture direction.

[c] Hybrid parameters, ibid. $S_{\Delta q}$ is the root mean square slope of the surface, S_{dr} the developed interfacial area ratio and S_{sc} the arithmetic mean summit curvature

[d] Functional parameters, ibid. S_{bi}, S_{ci} and S_{ci} are parameters describing the material ratio function.

autocorrelation function at half of its maximal height (used for the definition of the spacing) will be different. Therefore, the "spacing" parameters are in fact also "hybrid", i.e. they involve both amplitude and spatial information.

In statistics, methods are usually categorized by their *order* and can be also distinguished by the type of the data used in the calculation of the statistic (figure 2.1).

Order First order statistics describe the distribution of the height values in a single pixel, i.e. the probability of observing a certain height value in an arbitrary pixel. Second-order statistics consider pairs of pixels, i.e. they describe the probability of observing a height value pair in two pixels with a predefined relative position. Third order statistics involve three pixels, and so on. Higher order statistics describe multivariate distributions and are usually not feasible in practice. Image processing techniques involve many pixels, but describe only very specialized properties of the pixel distributions and do not give a detailed description of the distributions.

Data type While surface data is usually provided as continuous height values over a grid, some statistics require height values quantized to a small number of intervals. In image processing, the amplitude density function [31] is approximated by histograms, which count the number of pixels with amplitudes in distinct height intervals. Histograms are usually calculated with as few bins as possible to save computing time and space and to ensure statistical robustness of the statistics derived from them. Sometimes, only binary information is used: the statistics is based on the information if pixels exceed a certain threshold or not.

Figure 2.1 shows the categorization of the statistical methods regarding their order and input data type. In the following, these methods will be described in detail.

Abbott-Firestone curve The Abbott-Firestone curve (also called material ratio curve or bearing area curve) is equivalent to the estimated marginal distribution function of a random process. This curve is an important tool in surface characterization, and a large part of the surface characteristics defined in international standards [31] are derived from it (e.g. R_{vk}/S_{vk}) or have a direct relation (R_q/S_q, R_{sk}/S_{sk}, R_{ku}/S_{ku}). The Abbott-Firestone curve is a first-order statistic as it counts for every amplitude the relative number of pixel exceeding this height value, while spatial relations between two or more pixels are not taken into account.

In practical applications the Abbott-Firestone curve is used to predict the bearing behavior and the fluid retention properties of a surface. The

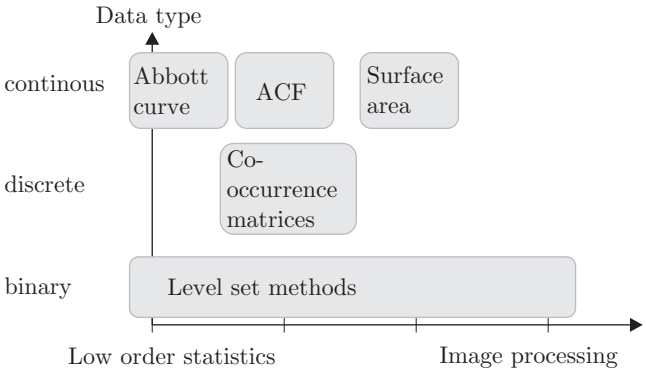

Figure 2.2.: Overview of statistical surface characterization methods.

bearing behavior of the surface helps to understand which stress a surface can withstand without being plastically deformed. Good fluid retention is required for the lubrication of a surface, as a surface which is able to store a fluid in cavities is expected to be less prone to galling in frictional contact [64, 87].

In both research and industrial practice, the Abbott-Firestone curve is gaining more and more importance: As it has become evident that the description of the surface microstructure in terms of an R_q/S_q is not sufficient for many applications, practitioners start to use also the additional information content of the complete Abbott curve. Its importance will be further underlined in the context of the methods introduced in chapter 3.

Autocorrelation function A method describing the distribution of height values of pixel pairs (second-order statistic) is the autocorrelation function (ACF). The ACF describes the correlation between two pixels at a given distance and direction [18]. The ACF always has a maximum in 0, as the correlation of a pixel with itself is maximal. Furthermore, the ACF decays toward longer distances between the two pixels compared[2]. A surface with large-scale structures will have a slower decay of its ACF as a surface with small structures. Therefore, the ACF can be used to express spatial properties of the surface. The ACF is often summarized in terms of

[2]There are mathematical reasons which require both statements to be fulfilled.

- its range S_{al}, i.e. the minimal length of its decay to half of its maximal value,
- its principal direction S_{td}, i.e. the direction of the slowest decay and
- its shape S_{tdr}, i.e. the ratio between the minimal and maximal length of its decay to half the maximal value.

Interestingly, also the root mean square slope $S_{\Delta q}$ is related to the ACF, as the following derivation shows:

$$
\begin{aligned}
S_{\Delta q} &= \sqrt{\frac{1}{|D|}\sum_{(i,j)\in D}\left(\frac{h_{i-1,j}-h_{i+1,j}}{2}\right)^2+\left(\frac{h_{i,j-1}-h_{i,j+1}}{2}\right)^2} \\
&= \sqrt{\frac{1}{4|D|}\sum_{(i,j)\in D} h_{i-1,j}^2-2h_{i-1,j}h_{i+1,j}+h_{i+1,j}^2+h_{i,j-1}^2-2h_{i,j-1}h_{i,j+1}+h_{i,j+1}^2} \\
&\approx \sqrt{\left(-A_{-2,0}/2+A_{0,0}-A_{+2,0}/2\right)/2+\left(-A_{0,-2}/2+A_{0,0}-A_{0,+2}/2\right)/2},
\end{aligned}
$$

where D is the measurement area, $h_{i,j}$ the height value over the grid point (i,j) and $A_{i,j}$ the estimated autocorrelation function's value at (i,j). Thus, the root mean square slope is an estimator for the autocorrelation function's curvature in $(0,0)$. Note that the approximation becomes sharp for large $|D|$.

Statistics of level sets A level set is the result of a thresholding operation, that is one cuts the surface at a given height and regards the points where the cutting plane hits the material as a set. Its complement is the region where the plane cuts through thin air. Thus, a level set $A_S(h)$ is the set of points in $\mathbb{R}^2$ at which the height of the surface S exceeds the height h (see also figure 3.1, chapter 3). Choosing a threshold above the highest surface peak yields an empty set; choosing a threshold below the deepest pit yields the full domain. The simplest feature of a level set is the relative area, also called the material ratio, which is the ratio between the material hit by the cutting plane and the area of the sampling window. The material ratio ranges from 0 to 1. Calculating the material ratio at different thresholds h yields the Abbott-Firestone curve.

Beyond the material ratio, other higher-order characteristics, which involve many pixels, can be calculated for level sets. One approach is to perform a segmentation of the level set into independent connected subsets and calculate statistics for these. For example, in [8] the mean area of the simply

connected subsets is used, while in [65], the area of the subsets connected to the border of the workpiece is considered to be useful. Both approaches lead to characterizing functions of a level set statistic as a function of the threshold.

If the surface data is interpreted as the realization of a random process, the level set is random and thus allows for the application of the whole mathematical theory of random closed sets [44, 54]. One of the preferred analysis tools for random closed sets are Minkowski measures, which will be described in detail in chapter 3, and contact distribution functions, which will be treated in chapter 4.

Co-occurrence matrices Statistical methods used in texture analysis, especially co-occurrence matrices, have also been applied in the context of surface microstructure characterization [97]. The co-occurrence matrices [26], a second-order statistics, describe the distribution of height value pairs for different relative distances and directions of the pixel pairs. As detailed in [32], the co-occurrence matrix $P_d(g, g')$ counts the number of pixel pairs which have intensities g and g' and where the second pixel is in position d relative to the first. To keep the matrices small and to provide a stable statistics, the scalar values are quantized to n levels, yielding $n \times n$ matrices. Also, d is often limited to neighboring pixels (usually from an 8 pixel neighborhood), resulting in 4 ($d = (1, 1), (0, 1), (-1, 1), (-1, 0)$) matrices. These matrices are again summarized in terms of simpler features such as their second moment, their average, etc.

Due to the quantization of the height values, the co-occurrence matrices perform a major information reduction; however, this might not be of interest for the description of directional features or spacing properties. Nevertheless co-occurrence matrices do not seem very useful for a specification of surfaces, since a direct physical interpretation of the calculated features is not given. Thus, their use will be limited to special applications, and might not find a widespread application compared to standardized parameters.

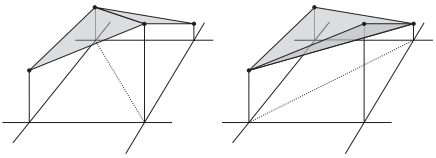

Figure 2.3.: The two possibilities of defining a triangulation of a surface over a rectangular lattice.

Surface area Though the meaning of the surface area is intuitively clear, it should be mentioned in the context of the other statistical parameters for completeness. The area of a two-dimensional manifold embedded in 3D can be calculated by integrating over the length of the normal vector, that is the vector perpendicular to the surface [14]. This is obviously not possible for data on a lattice, and therefore the surface area has to be approximated, usually by the cumulative area of the triangles spanned by three vertices of the height map over the lattice per triangle. For rectangular lattices, there is no unique way to choose these triangles (figure 2.3), and the surface has to be approximated by the mean over the two possible triangle combinations[3]. Each triangle involves three points and thus the surface area can be regarded as a third order statistics.

Statistical methods often have the disadvantage that their value does not correspond directly to a physical property of the data. Thus, the parameters' values are sometimes not easily interpretable. The root mean square slope $S_{\Delta q}$, for example, expresses the typical steepness of the surface slopes, but its absolute value does not have a direct physical meaning as other parameters, e.g. the density of summits S_{ds}, have. On the other hand, statistical parameters have the advantage that they are usually easy to calculate. Most of them can be expressed by mathematical formulas and accordingly, their behavior depending on the input data can be predicted. This allows for an analytical investigation of these parameters and properties like the change under the influence of measurement noise can be revealed.

2.2. Geometrical Methods

In contrast to statistical parameters, geometrical methods do not work directly on pixel tuples, but try to extract features like peaks or ridges from the surface and describe the features' properties and their spatial distribution. These methods are very natural and easy to understand, as they correspond to the human approach of data analysis: complex data sets are reduced to sets of objects which are analyzed further, neglecting irrelevant object features. Furthermore, the calculated parameters usually have an obvious physical meaning, which is often not the case with statistical methods.

As pointed out earlier in this section (p. 8), statistical methods cannot provide "spatial only" information, but always contain a mixture of amplitude and spacing. Feature-based methods, instead, can transform a 3D

[3] More accurate algorithms for the estimation of the real surface area can be devised, but the enhancement of the estimate does not make up for the calculation time.

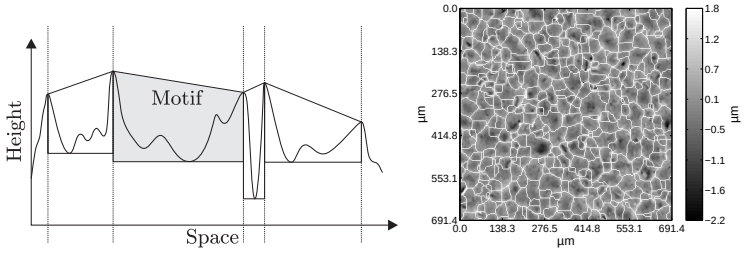

Figure 2.4.: Extraction of geometrical features in 2D (left) and 3D (right). The tessellation cells in the right image, marked by white lines, are the counterparts to the Motifs.

surface into a 2D point pattern (the extracted features positions), which describes spacing regardless of the features' amplitudes.

Although the extraction of features like peaks or dales from a surface is very natural, the exact definition of suitable algorithms is very problematic and has dragged on for more than a decade by now. The calculation of features requires far more complicated algorithms than the calculation of statistical parameters. The complexity of the algorithms comes with the necessity to prescribe the flow of control by conditions and control parameters. These control parameters have to be chosen heuristically, and this again means that the algorithms will be optimized for some typical surfaces but might lack generality.

Motif method The first geometrical method with a broad application in technical surface analysis, developed for profile data, was the Motif method [11, 31]. The idea behind the Motif method is to divide the profile into distinct sections. Starting with a sectioning given by local minima and maxima, these sections are recombined according to certain rules (fig. 2.4). Thus, the profile can be separated into distinct elements (the so-called motifs, corresponding to relevant valleys separated by peaks), which can be characterized by their geometrical properties.

3D feature extraction The extension of the Motif method to areal data is not straightforward at all and many approaches have been proposed [4, 5, 16, 66, 79]. The basic problems are that the simple definition of a peak of a profile cannot be transferred to 3D data, and that the shape of a Motif,

which is a segment for profile data, can be an arbitrary simply connected set for areal data. In general, the aim is to calculate a tessellation of the measurement area, that is a segmentation of the measurement area into distinct cells. The cell boundaries ought to follow significant topographic structures such as valleys, ridges or saddles. Details on the algorithms used can be found in [29, 78, 79]. In a second step, statistics over the cells' shape and position as well as statistics over geometrical properties of the features defined by the cells can be calculated. This approach is very general and many useful surface parameters can be derived in this way. One example of the application of this segmentation is the definition of the parameter S_z^{10}, which extends the profile parameter R_z, heavily used in industry, to 3D data (cf. chapter 6).

Most of the work dealing with geometrical analysis methods has far focused on how to calculate a robust segmentation of the height map. Yet, the analysis of the calculated cell structure is using only the most basic features like the number of cells. Analysis techniques for similar structures have been discussed in biological applications [7, 10] or astrophysics [48]. One basic idea is to analyze the point process which is dual to the cell structure, e.g. the point process formed by the cell centroids. Investigations include tests on complete spatial randomness, i.e. the independence of all points, or the homogeneity of the point patterns; literature abounds in contributions on the statistics of point processes, see e.g. [52]. Similar techniques making use of the mathematical framework of point processes will be used in chapter 4.

Unfortunately, 3D feature extraction, although under development for quite a long time, does not seem to have found its way into many practical applications yet. By reason of their historical prevalence, statistical parameters like the S parameter set are the preferred tool to this day due to their transparency regarding both implementation and data-dependent behavior.

2.3. Filter techniques and signal processing methods

The methods described in this section have in common that they do not perform a dimensionality reduction of the input data.

Filters are usually used to preprocess the acquired data to remove insignificant signal parts like the noise or to separate the different scales of the part. Therefore, they do not provide microstructure parameters directly, but meaningful parameters can be often calculated easily from filtered data by using simple operations like *mean*, *max* or *min*. As pointed out in [19], filter techniques are adequate for the description of the surface's geometry at

different scales, which is important in assembly problems, where functional properties related to friction etc. are of minor interest.

Data transforms just transform the data such that the information content is represented differently. This representation then reveals certain features of the data. In contrast to filters, transforms are reversible, i.e. the original data can be completely recovered from the transformed data.

Filters and signal processing methods can be divided into linear and nonlinear methods:

Linear methods Linear methods are the subject of linear systems theory [39]. The most important tool is the Fourier transform, which provides a global frequency decomposition of the data. The power spectrum derived from the Fourier transform expresses the energy of different frequencies in the signal, omitting their phase angle. It has been used extensively in surface microstructure analysis, for example to detect changes in the manufacturing process [45, 53, 98, 107].

Closely related to the Fourier transform is the wavelet transform. In contrast to the Fourier transform, it operates locally. Wavelet analysis performs a space-frequency decomposition: At any point in space a local spectrum is obtained. This makes wavelet analysis more suitable for non-stationary data. The second area of application of wavelets is its use as a matched filter: Positions where the surface is similar to the wavelet structure, i.e. show a high correlation with the wavelet used, yield high values in the wavelet transform. This allows for the identification of features like ridges or peaks by choosing an appropriate wavelet. Due to their flexibility and their usefulness for a wide range of applications, wavelets have become very popular in surface characterization tasks [33, 34, 37].

Linear methods have the advantage that they are based on a powerful and well-understood mathematical framework. Moreover, they can be calculated very efficiently using the Fast Fourier transform. However, these methods are not adequate for some phenomena, e.g. data containing sharp edges or outliers, or for non-stationary data.

Nonlinear methods While linear methods can be described independently of the input data – a linear filter can be defined by a transfer function –, nonlinear methods can only be understood for in the contex of a specific input signal. The most important nonlinear method for surface microstructure analysis is morphological filtering. The rolling ball filter [19, 42, 57] simulates a ball rolling over the height map. The new surface amplitudes are given by the lowest point of the ball. As the ball does not fit into narrow valleys, these will partly vanish in the filtered surface; the larger the radius of the ball,

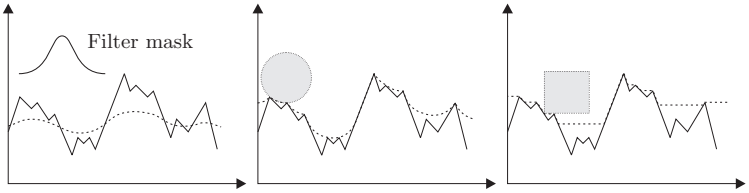

Figure 2.5.: Linear, rolling ball, and closing filter. The solid line is the unfiltered profile, the dashed line the filtered profile. The filters work analogously on 3D surface data.

the smoother the envelope (fig. 2.5). A lower envelope can be calculated analogously by fitting the rolling ball from below the surface. If a cube is used instead of a ball, the cube is not allowed to tilt – the filter result is equivalent to a morphological closing with a rectangular structuring element.

Similarly, other techniques from mathematical morphology as used in image processing [81], that is erosion, opening and closing etc. on gray value images can be used to filter the data. A detailed example of the usage of mathematical morphology for the definition of a roughness parameter is given in chapter 6, and advanced analysis techniques are proposed in chapter 4.

Nonlinear methods are usually less computationally efficient than linear methods. Their advantage over linear methods is the possibility to construct operators which ignore unwanted features in the data. Linear methods can attenuate these, but never completely remove them. For example, nonlinear filters can remove outliers regardless of their height, which is impossible with linear operators.

2.4. Model-based methods

Model-based methods are by and large a subgroup of the methods presented in the preceding sections. Some of the statistical, geometrical and filter/signal processing methods are also model based. Model-based methods assume that the observed data has generated according to a given model or according to given rules. Thus, these methods can also be used to simulate surfaces.

The model parameters determine the basic properties of the surface while random influence is required to generate realizations which share these basic properties. The model parameters therefore represent the most important

information content of a surface. The model can be constructed such that its parameters have a direct physical interpretation. For example, a surface could be modeled as a combination of peaks, with the number of peaks as the main model parameter. These parameters are thus very natural and easy to interpret. Likewise, machining parameters can be used as model parameters, thus covering the whole range of surfaces produced by the machining step.

Random field models Models for surfaces, especially random field models, are well-established [3, 60, 94]. The most basic random field model is one of independently and identically distributed amplitudes. If the distribution is simple enough (in practice, unimodal distributions will be sufficient in most cases), this distribution can be parameterized by its second to fourth moments. Thus, the parameters S_q, S_{ku} and S_{sk} which are estimates for these moments can be associated with the random field model. It also becomes clear that the mentioned parameters are most effective for surfaces resembling realizations of random fields, but will be less useful if calculated for surfaces with a deterministic structure.

Fractal methods Fractal methods seek to describe the roughness of a surface in terms of scale-independent characteristics such as the fractal dimension. A variety of methods for the extraction of these properties from surface data has been proposed [15, 17, 70].

The use of fractals has provoked a controversial discussion among researchers. One of the basic assumptions in fractal methods is the self-similarity of the surface, that is a similar appearance at different scales, thus admitting scale-independent properties. Following the arguments in [67, 99], this is definitely not the case for most engineering surfaces. Instead, surfaces *do* look different at different scales. For example, the form of the parts is deterministically shaped, but microstructure at nanometer scale is not. Moreover, the range of scales accessible by technical devices is usually far to small to justify the scale-independence assumption.

What can be observed in practice is that surfaces reveal more and more microstructure as the resolution is increased, and this observation has been mistaken for being *fractal* in many cases. The existence of arbitrary fine structure[4] is necessary for a fractal, but not sufficient. Accordingly, there is no need to stick to the self similarity assumption, as the observed behavior can be investigated by random processes of Markovian type. This concept has been introduced by [100], but does not seem to have found widespread applications yet [94].

[4] In reality, not even this applies, as every measurement is smooth at an atomistic level.

Wavelets Wavelet analysis is also based on a surface model, especially when used as a matched filter. One assumes that the surface under investigation contains a specific structure which coincides with the wavelet, and tries to extract these by using a wavelet tailored to ones needs [33, 34, 37].

The concept of surface models also plays a crucial role in the following chapters, where we will develop methods that allow to estimate model parameters for a broad range of surface models using a standard set of characteristics.

3. Minkowski functionals in the analysis of surface microstructure

In the preceding chapter, the outstanding importance of the Abbott-Firestone curve in research and practical applications has been underlined. The Abbott-Firestone curve allows for a stepwise information/data reduction, captures the characteristics of a surface in a compact way, and has a solid statistical foundation. Unfortunately, it captures no spatial information at all. In the following sections, a novel analysis technique, which is a direct generalization of the Abbott-Firestone curve is introduced: Section 3.1 shows how the Abbott-Firestone curve can be extended using techniques from stochastic geometry and how the new characterizing functions can be interpreted; section 3.2 illustrates how further parameters can be derived from these. The applicability of the proposed technique is demonstrated in chapter 5.

3.1. Stochastic geometry

3.1.1. The study of level sets

The study of level sets is another image processing technique that has proven its usefulness in many applications. A level set is the result of a thresholding operation, that is one cuts the surface at a given height and regards the points where the cutting plane hits the material as a set. Its complement is the region where the plane cuts through thin air. Thus, a level set $A_S(h)$ is the set of points in $\mathbb{R}^2$ at which the height of the surface S exceeds the height h (figure 3.1). Choosing a threshold above the highest surface peak yields an empty set; choosing a threshold below the deepest pit yields the full domain.

The simplest feature of a level set is the relative area, also called the material ratio, which is the ratio between the material hit by the cutting plane and the area of the sampling window. The material ratio ranges from 0 to 1. Calculating the material ratio at different thresholds h yields the material ratio curve (Abbott-Firestone curve, [1]), which is equivalent to the estimated marginal distribution function of a random process. This curve is an important tool in surface characterization, and a large part of the surface characteristics defined in international standards [31] are derived from it (e.g. R_{vk}) or have a direct relation (R_q, R_{sk}, R_{ku}).

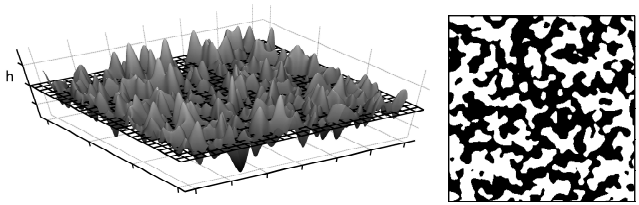

Figure 3.1.: A surface and a level set. The cutting plane is indicated by a mesh in the left image.

Complementary to the material area is the void area, the region where the cutting plane does not hit the material. This void area represents valleys, dales or cavities in the surface. The void area is of interest in tribology as cavities in the surface can serve as lubricant retention pockets. Several researchers [64, 68] have used the void area in their experiments. In their analysis, two kinds of void areas are distinguished: those which are connected to the border of the workpiece/ measurement window and those isolated from it. The resulting two area functions have been used in a number of tribological applications [8, 65].

Apart from the area, one can also investigate the contour length of the level sets. The contour length obviously contains information on how smooth the level set is. Sets with many or jagged objects will have a greater contour length than sets with a few smooth objects. The contour length of a level set at a fixed height has been used [36] to investigate the surface microstructure of sheet metal.

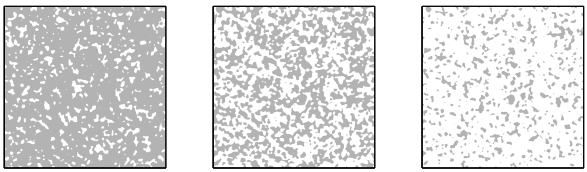

Figure 3.2.: Three 2D-sets with Euler characteristics $\chi = 395, 1, -371$, respectively. White areas represent material, gray represents void areas.

In addition to contour length and area, the number of isolated void areas

(i.e. cavities) or isolated material areas (i.e. peaks) is also of interest. It has been shown [101] that the number of isolated cavities, combined with their contour length and area, can be used to describe the frictional behavior of surfaces. The number of peaks of a surface has also been adopted by international standards [31, 29]. A similar quantity useful for counting objects is the so-called Euler characteristic χ, sometimes also called the genus, which counts the number of objects in a level set minus the number of holes in them (figure 3.2).

The Euler characteristic has an important interpretation in the context of percolation [50]. A negative Euler characteristic indicates that the material is predominantly characterized by isolated holes. Vice versa, for a positive Euler characteristic, the material would consist mainly of isolated objects. Thus, for a level set with a very low Euler characteristic, a fluid can be expected to be trapped in the holes, while it could flow freely in the case of a high Euler characteristic. Since the Euler characteristic relates to the possibility of fluid flow on a surface, it may be of great interest in tribological applications [82].

Area, contour length and the Euler characteristic of a 2D set are known in mathematics as Minkowski functionals[1]. In the following section, it will be pointed out in detail how these quantities can be used to describe surfaces.

3.1.2. Minkowski functionals

The Minkowski functionals, sometimes also called intrinsic volumes or Quermaß integrals, are functionals that describe the shape of sets in $\mathbb{R}^d$ [76][2]. For a set $\mathcal{C} \subset \mathbb{R}^2$, there exist three such functionals, namely the area A, the contour length C and the Euler characteristic χ which is the number of objects minus the number of holes. Surprisingly, the three functionals can be calculated in linear time for discrete binary sets by means of look-up tables (section 4.1.2). Especially the efficient calculation of the Euler characteristic is remarkable as it does not require complex image segmentation algorithms as one might expect. These three functionals have the following properties in common, as detailed in [49]:

- *Additivity*: For two sets $\mathcal{C}_1$ and $\mathcal{C}_2 \subset \mathbb{R}^2$, $m(\mathcal{C}_1 \cup \mathcal{C}_2) = m(\mathcal{C}_1) + m(\mathcal{C}_2) - m(\mathcal{C}_1 \cap \mathcal{C}_2)$.
- *Motion Invariance*: For any rotation ρ and any displacement t, $m(\rho\mathcal{C}_1 + t) = m(\mathcal{C}_1)$

[1] Strictly speaking, they are proportional to the Minkowski functionals, but the constants will be neglected here.

[2] Thresholding a height map yields a 2D set; hence, only the $d = 2$ case will be considered in the following.

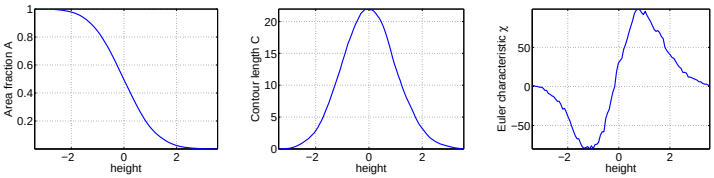

Figure 3.3.: The three characterizing functions for the surface example from figure 3.1.

- *Convex Continuity*: For a convex set $\mathcal{K}$ and a sequence of convex sets $\mathcal{K}_i$ approximating $\mathcal{K}$, also $m(\mathcal{K}_i) \to m(\mathcal{K})$,

where m is one of the functionals A, C or χ.

A famous theorem by Hadwiger [25] states that on the convex ring, every additive, motion invariant and convex continuous measure can be written as a linear combination of the Minkowski functionals. Thus, one can express every level set characteristic that is additive, motion invariant and convex continuous in terms of the Minkowski functionals only; other descriptors will be redundant. This completeness makes the Minkowski functionals a very important tool for describing sets. Minkowski functionals have been used to solve problems in areas ranging from materials science [62, 6] to astrophysics [48], which strongly encourages an investigation of their usefulness for surface data analysis.

3.1.3. Characterizing functions and their interpretation

As described in section 3.1.1, the Minkowski functionals can be calculated for all level sets $A_s(h)$, yielding three functions that can be used to characterize the surface. The area function is, up to normalization, simply the well known Abbott-Firestone curve, and the functions describing contour length and Euler characteristic can be seen as extensions thereof (figure 3.3).

The Abbott-Firestone curve is often summarized in terms of parameters related to its peak, core and valley part. Similarly, parameters can be derived from the contour length and Euler characteristic function:

- The contour length allows a deeper understanding of a surface's roughness than the Abbott-Firestone curve alone, as the latter does not take spatial information into account. The contour length function can be used to describe spatial features: For surfaces with smooth slopes it will have a lower amplitude than for surfaces with short-wavelength

structures. The latter will yield level sets with many small or jagged objects as the surface will cross the threshold very often. Thus, the maximal amplitude can be related to the spatial aspect of roughness (figure 5.2).

- For high thresholds, $\chi(u)$ is a good estimate for the number of peaks above this threshold. It is known that for Gaussian random functions, the Euler characteristic of a level set is the number of local maxima plus the number of local minima minus the number of saddle points above this threshold. As there are only a negliglible number of minima and saddle points above a high threshold, one can use the Euler characteristic to count peaks. The same result holds for low thresholds, where one can count pits.

- The Euler characteristic can also be used to define a percolation threshold as the height level where the Euler characteristic function has its zero crossing, according to the argument in section 3.1.1. Usually, there will be only one such height level (figures 5.1, 5.7). A high percolation threshold (it is supposed that the surface data has zero mean) suggests better fluid retention properties, as the fluid will not be able to move freely below this threshold [47, 46].

Overall, these parameters express surface properties in a condensed and interpretable form. However, in practical applications other, more specialized parameters may sometimes be of interest. For surfaces without observable structures, general statistical properties such as the covariance function are sufficient descriptors. On the other hand, for structured surfaces like ground surfaces or surfaces with embedded particles, the structures' properties, e.g. the number and shape of the troughs or particles are of interest. In the following section, it will be shown how the characterizing functions can be linked to such features. A systematic investigation is most easily performed using surface models, as these can be tailored to one's needs. A finite set of surfaces and the corresponding characterizing functions can be obtained from Monte-Carlo-simulation. But one can do better: For a broad class of surface models, the characterizing functions can be calculated analytically, giving a direct link between model parameters and characterizing functions.

3.2. Models for random surfaces

Once the relation between model parameters and characterizing function is known, the model parameters can be fit such that the deviation between analytically calculated and estimated Minkowski functionals is minimized.

The empirical Minkowski functionals can then be interpreted in the context of a specific model. Next, three random models especially suited for technical surfaces are introduced.

3.2.1. Random fields

The most frequently used and best established model for random surfaces is the random field model [60]. In this model, a random height value is assigned to each point of the reference plane[3] according to a joint distribution. The heights at different points are assumed to depend on each other, thus giving the possibility to model spatial features. In the following, only stationary and isotropic random fields will be considered. Stationary random fields have the same mean in each point, which is assumed to be 0 without loss of generality. That is, the mean over many realizations is 0 in every point. Isotropy means that the relation between two points depends only on their distance but not on the direction of the second point relative to the first. In the following, two important special cases of random fields will be considered:

- Gaussian random fields (GRF) follow a multivariate Gaussian distribution. For a stationary and isotropic GRF, this multivariate distribution can be completely characterized by its covariance function, which depends only on the distance between two points. The use of GRF is often motivated by the central limit theorem of probability theory which states (roughly) that the sum of arbitrary independent random variables tends to a Gaussian distribution. This assumption often applies to practical situations where the machining process consists of many independent events, e.g. in shot-blasting.

- In χ^2 random fields[4], the heights are distributed according to a χ^2 distribution with N degrees of freedom. A χ^2 distribution is the sum of N squared Gaussian distributions. For small N, this distribution is asymmetric; for large N, it tends to a Gaussian distribution. The χ^2 field is of interest because it allows us to model asymmetric distributions. It has been investigated in [3].

- Similar to the χ^2 field, other random fields derived from the Gaussian allow for an analytical investigation. These fields will not be considered here; details can be found in [74, 106].

[3] As surface measurements are usually recorded as data on a lattice, the points can be assumed to lie on a grid, corresponding to the pixels of a height map.

[4] The χ in "χ^2 random fields" should not be confused with the Euler characteristic which is also denoted by χ. There is no relation between the two.

All the random function models mentioned above are derived from the GRF. Other distributions of practical interest exist, but none of these seem to be theoretically tractable to the extent of the distributions related to the Gaussian. The latter seem to be adequate for the modeling of a wide range of phenomena.

3.2.2. Markov random fields

Due to their specific properties, we will treat Markov random fields separately, though they are a special case of the general class of random fields introduced above.

A MRF is a family of random variables S_{ij} with integers i and j denoting the pixel (i, j). Each random variable is surrounded by a set of neighbors

$$\partial(S_{ij}) = \{S_{km} | (i, j) \text{ and } (k, m) \text{ are adjacent pixels}\}.$$

For rectangular lattices, a 4- or 8-neighborhood can be chosen; the 4-neighborhood includes only directly adjacent pixels, while the 8-neighborhood includes also diagonal adjacent pixels. In the following, we will use the 4-neighborhood $\partial(S_{ij}) = \{S_{i-1,j}, S_{i+1,j} S_{i,j-1} S_{i,j+1}\}$.

A MRF's probability density $P(S)$ is then defined by the two properties [103]

1. **Positivity:** $P(S = s) > 0$.
   The probability of observing an arbitrary s is nonzero.

2. **Markov property:** $P(S_{ij} | \{S_{kl}, (k, l) \neq (i, j)\}) = P(S_{ij} | \partial(S_{ij}))$
   The distribution of a random variable depends only on the values of its neighbors.

With these properties, it can be shown (Hammersley-Clifford theorem, [38]) that the probability density of S is a Gibbs field

$$P(S = s) = \frac{1}{Z} \exp\left(- \sum_{c_1, c_2 \in C} V_{c_1, c_2}(s_{c_1}, s_{c_2}) \right), \tag{3.1}$$

where C is the set of adjacent pixel pairs regarding the 4-neighborhood, s a realization of S and $V_{c_1,c_2} : \mathbb{R}^2 \rightarrow \mathbb{R}$ the so-called potential functions. The normalizing constant Z is also called *partition function*. The potential functions are given by $V_{c_1,c_2}(s_{c_1}, s_{c_2}) = log(P(s_{c_1} | s_{c_2}))$.

An important special case [12] is the generalized Gaussian model

$$V_{c_1,c_2}(s_{c_1}, s_{c_2}) = -b \left(\frac{s_{c_1} - s_{c_2}}{\sigma_V} \right)^p, 0 < p. \tag{3.2}$$

For $p = 2$, the Gibbs field (3.1) is a multivariate Gaussian density.

3.2.3. Boolean models

Random fields model the height distribution in every point of the reference plane; relations between neighboring points are given by a joint distribution. This assumption is not adequate for some surface topographies. For example, consider a ground surface which consists of plateaus separated by troughs. The direction and depth of the troughs will be random, but as one moves along the bottom of a trough, it is clear that the next point will have the same height as the current point. Such a behavior cannot be expressed by random fields, as relations between neighboring points would always be random. The Boolean model, instead, offers the possibility to model randomly located deterministic objects, as observed in the ground surface example.

The Boolean model is based on a Poisson point process, that is a number of points chosen at random from $\mathbb{R}^2$. At each of these random locations (also called *germs*), a 3D-object (called a *grain*) of random shape and rotation is placed[5]. Associating to each point in $\mathbb{R}^2$ the maximum of all objects heights in this points yields a 2D-surface embedded in $\mathbb{R}^3$.

In figure 5.7, two examples of Boolean models are shown. The right is the trough model mentioned above, while the left is a realization of a Boolean model consisting of cylinders of random heights with spherical caps. This model corresponds to the famous Greenwood-Williamson model of surfaces [24]. Greenwood and Williamson model the surface as asperities with a spherical cap having a Gaussian height distribution. Each of these asperities can be seen as a grain of a Boolean model. The grains' height distribution can be chosen to be Gaussian.

3.2.4. Minkowski functionals of random surface models

For the models presented above, it is possible to calculate the expected Minkowski functionals in terms of the models' parameters. In the following, h will denote the height of the level set.

[5] The original definition of Boolean models uses a point process in $\mathbb{R}^n$ and $\mathbb{R}^n$-grains. The union of all grain yields a $\mathbb{R}^n$ random set. For a detailed definition of Boolean models and its variants, see e.g. [55].

Gaussian random fields For isotropic stationary zero-mean GRFs with certain smoothness constraints, the analytical formulae for the expected Minkowski functionals are [2, 89]

$$\begin{aligned} A(h) &= \Phi\left(\tfrac{h}{\sigma}\right) \\ C(h) &= \tfrac{\sqrt{|\tau|}}{2}\exp\left(-\tfrac{h^2}{2\sigma^2}\right) \\ \chi(h) &= \tfrac{h}{\sqrt{2\pi}\sigma}\tfrac{|\tau|}{2\pi}\exp\left(-\tfrac{h^2}{2\sigma^2}\right) \end{aligned} \tag{3.3}$$

where Φ denotes the standard normal distribution, σ the standard deviation and τ the second derivative in 0 of the normed covariance function. Note that the area function depends only on the standard deviation σ, while contour length and Euler characteristic are determined only by σ and the second derivative of the covariance function. Hence, in the special case of GRF, the Euler characteristic does not provide more information than the contour length. In practice, however, data sets usually will not be exactly Gaussian, and both functions should be considered.

χ^2 fields For χ^2 fields with N degrees of freedom, one gets [74]

$$\begin{aligned} A(h) &= 1 - P\left(\tfrac{h}{2\sigma}, \tfrac{N}{2}\right) \\ C(h) &= \tfrac{\pi\sqrt{|\tau|}}{2\Gamma(\frac{N}{2})}\left(\tfrac{h}{2\sigma}\right)^{\frac{N-1}{2}}\exp\left(\tfrac{-h}{2\sigma}\right) \\ \chi(h) &= \tfrac{|\tau|}{2\pi\Gamma(\frac{N}{2})}\left(\tfrac{h}{2\sigma}\right)^{\frac{N-2}{2}}\exp\left(-\tfrac{h}{2\sigma}\right)\left(\tfrac{h}{\sigma} - (N-1)\right), \end{aligned} \tag{3.4}$$

where N is the number of degrees of freedom of the χ^2 distribution, $\Gamma(a) = \int_0^\infty e^{-t}t^{a-1}dt$ the Gamma function, $P(x,a) = \frac{1}{\Gamma(a)}\int_0^x e^{-t}t^{a-1}dt$ the incomplete Gamma function, σ the standard deviation and τ the second derivative of the covariance function in 0 of the underlying GRF.

Similar expressions for other random fields related to GRF can be derived using the formulae in [74, 106].

GRFs are determined completely by their standard deviation and their covariance function, which describes the correlation between pairs of pixels. For stationary random fields on $\mathbb{R}^2$, the covariance function is a function of $x \in \mathbb{R}^2$, the difference vector between two locations x_1 and x_2. For rotation-invariant fields, the covariance function simplifies to a function of the distance $|x_1 - x_2|$, thus being a function defined on $\mathbb{R}^+$. The following considerations are limited to the rotation-invariant case.

The covariance function, which can be estimated by the autocorrelation function, describes the scales of the surface. Its values around 0 are related to short-range (high frequency) behavior; long range features (low frequency) influence more distant values. Thus, the roughness of the surface will mainly have impact on the covariance function around the origin.

Different covariance functions can result in remarkably different surfaces (see fig. 5.2), even if the marginal distributions are identical. The shape of the covariance function cannot be arbitrary, but is limited to the quite restricted class of positive definite functions [71]. Roughly speaking, positive definiteness means that the covariance matrices of any finite subset of random variables must be positive semi-definite, since the fields probability density involves its inverse. One necessary condition is that none of a covariance function's values be greater than its value at the origin.

In the following, important examples for covariance functions are listed. The covariance functions together with simulation examples are plotted in figure 5.2. In the context of stochastic geometry, one is especially interested in the covariance functions' second derivative in 0, as evident from equation (3.3). The respective expressions are given below. The larger the second derivative's absolute value, the steeper the covariance function in 0, which in turn is a sign of the dominance of high frequencies or very rough, jagged surfaces.

- The **powered exponential covariance function** is defined as

$$\mathcal{C}(x) = \exp\big(-\frac{x^\eta}{2\nu^2}\big), \eta \in (0, 2). \tag{3.5}$$

  This function is not twice differentiable in 0 and has a sharp peak in 0. As a consequence, the power spectrum of such a GRF is known to decay only slowly towards high frequencies, and the GRF will reveal ever more detail when sampled with a higher sampling rate. Thus, exponential covariance can be used to model fractal-like surface. The covariance functions' peak at the origin can be interpreted as having an infinite second derivative; as also the contour length of the fractal-like level sets are not finite, formula (3.3) remains consistent with this interpretation.

- Setting $\eta = 2$ in the above equation yields the **Gaussian covariance function**

$$\mathcal{C}(x) = \exp\big(-\frac{x^2}{2\nu^2}\big) \text{ with } \frac{\partial \mathcal{C}}{\partial^2 x}(0) = -\frac{1}{\nu^2}. \tag{3.6}$$

  Also the power spectrum of the realizations will have a Gaussian shape. Hence, GRFs with a Gaussian covariance type will contain presumably

low frequencies, and will be smooth on very small scales as the amplitudes of high frequencies decay exponentially.

- The **Cauchy covariance function** is defined by

$$\mathcal{C}(x) = (1 + x^2)^{-\nu} \text{ with } \frac{\partial \mathcal{C}}{\partial^2 x}(0) = -2\nu. \tag{3.7}$$

  This covariance function decays rapidly in the vicinity of 0 but only very slowly at longer distances (fig 5.2). This behavior is similar to the exponential covariance function and hence, realizations contain both large-scale structures as well as a very rough structure at small scales.

- **Bessel type covariance function**

$$\mathcal{C}(x) = 2^\nu \Gamma(\nu + 1) x^\nu J_\nu(x), \nu \geq 0 \text{ with } \frac{\partial \mathcal{C}}{\partial^2 x}(0) = -\frac{1}{2(\nu + 1)}, \tag{3.8}$$

  where J_ν is a Bessel function and Γ is the Gamma function. The Bessel type covariance function differs from the functions presented above as it can also adopt negative values. Its general shape is an oscillation around the x-axis with decaying amplitude. The power spectrum will be limited to a short frequency range. Accordingly, the surface will show quasi-deterministic, grain-like structures with arbitrary orientations but a typical size related to ν.

A detailed treatment of these covariance functions, as well as methods to construct further covariance functions can be found in [71].

Markov random fields Expectations for the Minkowski functionals are calculated over a continuous domain. Markov random fields, instead, are defined on a lattice. However, the MRF can be seen as a smooth random field R on $\mathbb{R}^2$ sampled at the lattice points.

Note that a random field defined over a continuous domain is of Markov type it has an exponential covariance function [22]. As detailed above, such a random field would not admit the calculation of the Minkowski functionals.

Nevertheless, for the smooth random field R behind the MRF S, the Minkowski functionals can be calculated. To this end, we assume that R is obtained by interpolation of S such that the distributions of amplitudes of its first and second derivatives estimated from S using the standard estimators from in image processing coincide with the respective distributions for R. This is a technical assumption which assures that S and R coincide in the basic properties necessary for the calculation of the Minkowski functionals.

Then, one can replace the amplitude density and derivatives' distributions of R, the field for which the Minkowski functionals can be defined, by the respective distributions estimated from S. This is all what is needed for the estimation of the Minkowski functionals from measurement data (section 4.1.2).

For MRFs with a Gaussian potential function, the estimated Minkowski functionals are in accordance with equation (3.3) as the MRF is a Gaussian random field in this case. As experimental results in section 5.2.2 show, the characterizing functions for non-Gaussian MRFs behave similar to characterizing functions of Gaussian random fields, but the amplitudes of the contour length function and Euler characteristic function are additionally influenced by p, the parameter determining the shape of the potential function.

Boolean models For Boolean models [96], the equations

$$\begin{aligned} A(h) &= 1 - \exp\left(-\rho\bar{A}(h)\right) \\ C(h) &= \tfrac{2}{\sqrt{\pi}} \exp\left(-\rho\bar{A}(h)\right) \rho\bar{C}(h) \\ \chi(h) &= \exp\left(-\rho\bar{A}(h)\right) \left(\rho\bar{\chi}(h) - \tfrac{1}{4\pi}\rho\bar{C}(h)\right). \end{aligned} \tag{3.9}$$

hold, where ρ is the density of the underlying point process and $\bar{A}(h)$, $\bar{C}(h)$ and $\bar{\chi}(h)$ denote the area, the contour length and the Euler characteristic of the typical grain.

In the Boolean grain model, the single grains have in general not a unique shape, but each grain looks different; each grain is a set-valued realization of a random process. Here, these sets are only described by their area, contour length and Euler characteristic. If one deals with simply connected grains only, $\bar{\chi}(h)$ is constant 1. Now, the expectations for the area, contour length and Euler characteristic of the mentioned set-valued process can be calculated. These expectations are $\bar{A}(h)$, $\bar{C}(h)$ and $\bar{\chi}(h)$, the description of what is called the *typical grain*. It is important to note that these quantities are expectations, but not descriptors of a single set. For example, consider circular grains with radius r distributed uniformly on $[a, b]$. Then, the characteristics of the typical grain are given by

$$\bar{A} = \frac{1}{b-a}\int_a^b r^2\pi dr = \frac{\pi}{3}(b^2 + ab + a^2)$$

and

$$\bar{C} = \frac{1}{b-a}\int_a^b 2r\pi dr = \pi(b^2 - a^2).$$

Obviously, $\bar{A}$ and $\bar{C}$ are not the area and contour length of a circular grain. This simple example highlights how the concept of the *typical grain* has to be understood.

For every h, (3.9) is an equation system with four unknown variables, that is (3.9) is under-determined. In practice, often simply connected grains (e.g. structures obtained from sections through single asperities, bowl-shaped grains etc.) with $\chi = 1$ can be assumed, and the equation system can be solved for ρ, $\bar{A}(h)$, $\bar{C}(h)$.

However, this assumption might be violated in practical applications: Real surfaces are never completely smooth, and also measurement noise will add artifacts like local minima. Cutting such a surface at a given height level will yield grains with holes, violating the assumption of $\chi = 1$. Thus, in order to successfully apply the Boolean grain model interpretation, the measurement data will have to be preprocessed in order to restore the smooth, simply connected grains. Examples for these difficulties and proposals for countermeasures are given in chapter 5. The effects of typical image processing filters will be studied in chapter 4.

3.2.5. Synopsis

Having equations 3.3–3.9 at hand, the influence of a surface's properties on its characterizing functions becomes clear immediately. It is obvious, for example, that in the case of a surface resembling the realization of a GRF, the material ratio depends only on the standard derivation of the underlying Gaussian distribution; both the contour length and Euler characteristic depend on the second derivative of the covariance function in 0. Thus, contour length and Euler characteristic make it possible to distinguish surfaces with same marginal distribution but different covariance functions. The Minkowski functionals of Boolean models, instead, depend only on the number of grains and the shape of the typical grain.

Vice versa, it is possible to estimate these parameters from the characterizing functions of real data by fitting an appropriate model in terms of the expected characterizing functions. If one assumes the typical grain to be simply connected, thus having a Euler characteristic $\bar{\chi}(u) \equiv 1$, the number of grains and the area and contour length of the typical grain can be uniquely determined from the characterizing functions, which is difficult to achieve by other methods. For Gaussian random fields and χ^2-fields, it would already be sufficient to fit the contour length function: its amplitude is related only to τ, while its extent along the height axis corresponds to the standard deviation of the random function. Nevertheless, it is more informative to fit all three characteristic functions, as this will provide us with more stable results. Furthermore, one can also check how well the empirical functions

and the analytically calculated ones match. The selected surface model is tenable only if all three empirical functions match the theoretical well.

4. Practical issues and extensions of the characterizing functions

4.1. Practical issues

This section covers various topics which concern the practitioner who wants to apply the methods proposed in chapter 3.

4.1.1. Estimation of the Minkowski functionals from multiple measurements

Beyond the arguments for the usefulness of the characterizing functions given in section 3.1.3, another advantage for practical applications stems from the additivity and rotation-invariance of the Minkowski functionals. Suppose the user has acquired several measurements of a surface which do not overlap, and are positioned arbitrarily on a part's surface. This occurs frequently in practical applications, since it is often not possible to measure the whole surface at once. Especially when using optical measurement systems, the measurement area cannot be enlarged arbitrarily due to restrictions of the optics and the camera system.

To recompose the whole surface, it is therefore necessary to stitch the single measurement windows. However, this is not necessary for the calculation of the Minkowski functionals. As the Minkowski functionals' values do not depend on the rotation angle of the data, the Minkowski functionals of the single measurement windows can simply be added. Thus, the use of the Minkowski functionals allows for the enlargement of the measurement window without performing complicated stitching operations. This can be used to acquire statistically more robust information on a surface's microstructure.

4.1.2. Estimation of the characterizing functions

For a successful application of the proposed characterizing functions in an industrial environment it is important to provide unambigous definitions for their computation. This is extremely important if one thinks about standardization. Any ambiguity in the calculation rules will lead to deviant results for different implementations, and the standard would become useless.

Although area, contour length and Euler characteristic are clearly defined for sets in $\mathbb{R}^2$, they have to be estimated from measurement data, which provides only amplitudes on a discrete grid for a measurement window of limited size[1]. Various estimators have been proposed [61, 74, 35, 59, 102, 23, 20]; after reviewing the estimator used most often in image processing, a novel accurate and fast estimator for the characterizing functions is proposed.

Estimators on level sets

The straightforward approach to calculate level set features is to use thresholding to transform the height map into a binary image. This binary image has the value 1 where the amplitude in a pixel exceeds the threshold and is 0 elsewhere. Gray [23] proposes an algorithm based on local binary patterns for the calculation of area, contour length and Euler characteristic.

A local binary pattern is a 2×2 array of adjacent pixels. Such a matrix can be in one of 16 configurations; grouping configurations that are equivalent up to rotation yields five groups Q_i

$$Q_0 = \begin{bmatrix} 0 & 0 \\ 0 & 0 \end{bmatrix}, Q_1 = \begin{bmatrix} 1 & 0 \\ 0 & 0 \end{bmatrix}, Q_2 = \begin{bmatrix} 1 & 1 \\ 0 & 0 \end{bmatrix},$$

$$Q_3 = \begin{bmatrix} 1 & 1 \\ 1 & 0 \end{bmatrix}, Q_4 = \begin{bmatrix} 1 & 1 \\ 1 & 1 \end{bmatrix},$$

each containing exactly i pixels with value 1. Another group Q_D containing two pixels with value 1 is given by the configurations

$$\begin{bmatrix} 1 & 0 \\ 0 & 1 \end{bmatrix} \text{ and } \begin{bmatrix} 0 & 1 \\ 1 & 0 \end{bmatrix}.$$

It is easy to prove that the area A and contour length C can be estimated by

$$\begin{aligned} A &= (\sharp Q_1 + 2\sharp Q_2 + 2\sharp Q_D + 3\sharp Q_3 + 4\sharp Q_4)/4 \\ C &= \sharp Q_1 + \sharp Q_2 + 2\sharp Q_D + \sharp Q_3, \end{aligned} \tag{4.1}$$

where $\sharp Q$ denotes the number of configurations Q in the binary image. Unfortunately, these estimators are not very accurate. For example, the configuration Q_D contains 2 pixels with value 1; this adds 2 to the value of C if one calculates the contour length by counting the number of border pixels

[1] The contour length is the integral along the boundary of the level set over 1, and the Euler characteristic is proportional to the integral along the contour over the mean curvature [69, 77].

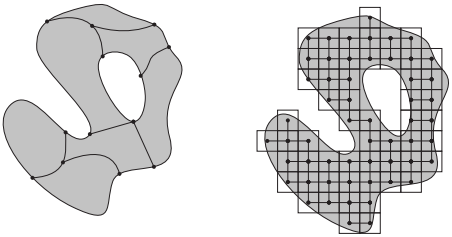

Figure 4.1.: Calculation of the Euler characteristic by tesselation of an object. The left image shows the tesselation of an arbitrary set; the right image shows the tesselation of a binary image, where the pixels are indicated by squares each containing a graph vertex.

as in (4.1). However, as Q_D is representing a diagonal, $\sqrt{2}$ would be more accurate. Based on similar considerations, (4.1) can be refined [20] to

$$\begin{aligned} A &= \frac{1}{8}\sharp Q_1 + \frac{1}{4}\sharp Q_2 + \frac{1}{4}\sharp Q_D + \frac{7}{8}\sharp Q_3 + \sharp Q_4 \\ C &= \sharp Q_2 + \frac{1}{\sqrt{2}}(\sharp Q_1 + 2\sharp Q_D + \sharp Q_3). \end{aligned} \tag{4.2}$$

To calculate the Euler characteristic by means of local binary patterns, we have to review some basic graph theory. It is a well known fact that for a simply connected planar graph the equation

$$n_V - n_E + n_F = 1 \tag{4.3}$$

holds, where n_V is the number of vertices, n_E the number of edges and n_F the number of faces[2]. If a planar graph can be decomposed into simply connected subgraphs, $n_V - n_E + n_F$ gives the number of subgraphs. If the cells of the graph are colored with 0 or 1 and n_V, n_E and n_F are counted for cells colored with 1 only, $n_V - n_E + n_F$ counts the number of objects (areas colored with 1 surrounded by areas colored with 0) minus the number of holes (areas colored with 0 surrounded by areas colored with 1), which is the Euler characteristic. Vice versa, the Euler characteristic for a set in $\mathbb{R}^2$ can be calculated by choosing an arbitrary tesselation of the set and counting the number of vertices, edges and cells in the set (figure 4.1).

This idea can be adopted to calculate the Euler characteristic of binary

[2]The outer infinitely large region is not counted as a face.

images. To each pixel in the level set (pixels with value 1) a vertex is assigned, and each pixel is connected to its neighbors by edges. Depending on the chosen neighborhood (4- or 8-neighborhood), each vertex can have at most 4 or 8 neighbors. To count the numbers n_V, n_E and n_F, local binary patterns can be used. The patterns Q_i, $0 \leq i \leq 4$ contribute i vertices, and Q_D contributes 2 vertices to n_V; as the local binary patterns overlap, each vertex will be added four times, and therefore

$$n_V = (\sharp Q_1 + 2\sharp Q_2 + 2\sharp Q_D + 3\sharp Q_3 + 4\sharp Q_4)/4. \tag{4.4}$$

The number of edges depends on the chosen neighborhood: For a 4-neighborhood, diagonally adjacent pixels do not contribute an edge; again, the edges are counted doubly, and we obtain

$$n_E^{(4)} = (\sharp Q_2 + 2\sharp Q_3 + 4\sharp Q_4)/2. \tag{4.5}$$

In the case of an 8-neighborhood, there are also diagonal edges (these are not counted doubly), and

$$n_E^{(8)} = \sharp Q_2/2 + \sharp Q_D + 2\sharp Q_3 + 3\sharp Q_4. \tag{4.6}$$

Similarly, we get

$$\begin{aligned} n_F^{(4)} &= \sharp Q_4 \text{ and} \\ n_F^{(8)} &= \sharp Q_3 + 2\sharp Q_4 \end{aligned} \tag{4.7}$$

for the respective neighborhoods. Combining eqs. (4.4-4.7) yields

$$\begin{aligned} \chi^{(4)} &= (\sharp Q_1 + 2\sharp Q_D - \sharp Q_3)/4 \text{ and} \\ \chi^{(8)} &= (\sharp Q_1 - 2\sharp Q_D - \sharp Q_3)/4. \end{aligned} \tag{4.8}$$

These estimators are biased in opposite directions [74, 63]; the mean value

$$\chi = (\sharp Q_1 - \sharp Q_3)/4 \tag{4.9}$$

yields a better estimate, but is still biased.

Estimators working directly on the gray-level image

Surprisingly, the three characterizing functions can be estimated without having to explicitly calculate the level sets first.

Let us start with the area ratio function: it is well known that the area

ratio is an estimator for the cumulative marginal distribution function. For a random function R defined over a domain D, this function can be estimated by

$$\hat{A}(h) = \frac{1}{|D|} \int_{\{x \in D : R(x) \leq h\}} 1 dx \tag{4.10}$$

or, for a random function sampled on a rectangular lattice with $N < \infty$ vertices, by

$$\hat{A}(h) = \frac{1}{N} \sum_{\{x \in D : R(x) \leq h\}} 1, \tag{4.11}$$

where D is limited to lattice vertices.

Sorting the pixels regarding their amplitudes yields a list of distinct values $h_1, \ldots, h_m$, $m \leq N$. Hence, we have

$$\begin{aligned} \hat{A}(h_k) &= \left(\sum_{i=2}^{k} \hat{A}(h_i) - \hat{A}(h_{i-1}) \right) + \hat{A}(h_1) \\ &= \frac{1}{N} \sum_{i=1}^{k} |\{x \in D : R(x) = h_i\}|. \end{aligned} \tag{4.12}$$

That is, one has to sort all pixels regarding their height values, count the pixels with equal amplitudes, and compute the cumulative sum. This gives us $\hat{A}$ sampled at $h_1, \ldots, h_m$. For $h \notin \{h_1, \ldots, h_m\}$, $\hat{A}$ can be interpolated.

A similar procedure can be used to calculate contour length and Euler characteristic. According to [89], the contour length of a level set can be estimated by

$$\hat{C}(h) = \frac{1}{|D|} \int_{\partial A_R(h)} 1 ds, \tag{4.13}$$

where ds denotes the path integration along the border $\partial A_R(h)$ of the level set $A_R(h)$. The path integral can be calculated by integrating over the gradient $|\nabla R(x)|$ in all boundary points of $A_R(h)$, and thus

$$\hat{C}(h) = \frac{1}{|D|} \int_D \delta(R(x) - h) |\nabla R(x)| dx, \tag{4.14}$$

where δ is 1 if h equals $R(x)$ and else is 0. Calculating the δ operator for each pixel implicitly means calculating the level set. This can be avoided by

integrating over h on both sides:

$$\begin{aligned}\hat{C}_{int}(h) &= \int_{-\infty}^{h} \hat{C}(\nu)d\nu \\ &= \frac{1}{|D|}\int_D \int_{-\infty}^{h} \delta(\nu - R(x))d\nu|\nabla R(x)|dx \\ &= \frac{1}{|D|}\int_{\{x\in D:R(x)\leq h\}} |\nabla R(x)|dx. \end{aligned} \tag{4.15}$$

$\hat{C}$ can later be recovered by calculating the derivative of $\hat{C}_{int}(h)$. Now, the right hand side of (4.15) takes the same form as equation (4.10), and we can use a cumulative sum to estimate $\hat{C}_{int}$ without explicitly calculating level sets. In practice, (4.15) can again be approximated by a sum

$$\hat{C}_{int}(h_k) = \frac{1}{N}\sum_{i=1}^{k} \sum_{\{x\in D:R(x)=h_i\}} |\nabla R(x)|, \tag{4.16}$$

where the gradient $|\nabla R(x)|$ can be estimated from a 3×3 neighborhood centered at x[3].

The same trick can be used to estimate the Euler characteristic, defined using the integral over the curvature κ along the level set's boundary $\partial A_R(h)$ [89][4]. Thus,

$$\hat{\chi}(h) = \frac{1}{2\pi|D|}\int_{\partial A_R(h)} \kappa(x)ds, \tag{4.17}$$

and

$$\hat{\chi}_{int}(h) = \frac{1}{2\pi|D|}\int_{\{x\in D:R(x)\leq h\}} \kappa(x)|\nabla R(x)|dx. \tag{4.18}$$

The curvature κ of the level set can be expressed by first and second derivatives of the original surface:

$$\kappa(x) = \frac{2R_{12}R_1R_2 - R_1^2R_2 - R_2^2R_{11}}{|\nabla R(x)|^{3/2}}, \tag{4.19}$$

[3] In theory, the surface might not be differentiable in every point, as it is the case for a GRF with exponential covariance function (eq. (3.5)). In practice, however, the surface is sampled only on a lattice, and as long as all amplitudes are finite, the derivatives can always be estimated. We can therefore savely ignore the mathematical difficulties arising for non-differentiable surfaces.

[4] The integral over the curvature of a circle would yield 2π, so we have to divide by 2π to get the Euler characteristic.

where $R_{ab} = \frac{\partial R}{\partial a \partial b}(x)$ denotes the derivative with respect to directions a and b. The argument x is omitted for simplicity. In practice, the integral is approximated by the sum

$$\hat{\chi}_{int}(h_k) = \frac{1}{2\pi N} \sum_{i=1}^{k} \sum_{\{x \in D : R(x) = h_i\}} \kappa(x) |\nabla R(x)|. \tag{4.20}$$

Formulae (4.14) and (4.17) are exact expressions for the expectations of the contour length and Euler characteristic for $|D| \to \infty$ [2, 89]. The actual quality of the estimators is hence only limited by the restriction to a finite lattice.

It should be noted that the calculation of $\frac{\partial \hat{C}_{int}}{\partial h}$ is not trivial in practice: Both functions are usually jaggy, eventually leading to noisy $\hat{C}$ and $\hat{\chi}$ if not evaluated carefully.

In order to calculate $\hat{A}$, $\hat{C}_{int}$, $\hat{\chi}_{int}$ according to (4.12), we have to sort the height values to obtain $h_1, \ldots, h_m$. This is an $O(N \log N)$ step; the further steps will cost only $O(N)$. Remarkably, even for a small number K of level sets, the proposed algorithm's complexity is lower than the straightforward calculation on the level sets, which is of complexity $O(NK)$.

To conclude this section, the algorithm for the calculation of $\hat{A}$, $\hat{C}$ and $\hat{\chi}$ is summarized:

1. Calculate $|\nabla R(x)|$ and $\kappa(x)|\nabla R(x)|$ for every $x \in D$ based on local neighborhoods.

2. Sort the height map R to get $h_1, \ldots, h_m$. For every h_i, this yields a set $D_i = \{x \in D : R(x) = h_i\}$.

3. Calculate the cumulative sums

   - $\hat{A}(h_k) = \frac{1}{N} \sum_{i=1}^{k} |D_i|$
   - $\hat{C}_{int}(h_k) = \frac{1}{N} \sum_{i=1}^{k} \sum_{x \in D_i} |\nabla R(x)|$
   - $\hat{\chi}_{int}(h_k) = \frac{1}{2\pi N} \sum_{i=1}^{k} \sum_{x \in D_i} \kappa(x) |\nabla R(x)|$

4. Recover $\hat{C}$ and $\hat{\chi}$ by numerically differentiating $\hat{C}_{int}$ and $\hat{\chi}_{int}$.

4.1.3. Comparison of the characterizing functions with existing surface microstructure parameters

When proposing a new characterization technique, it is necessary to compare it to established techniques. In areal surface characterization, the most

established and quasi-standardized technique is the calculation of the S-parameter set (also referred to as the Birmingham-14 parameter set by some authors) proposed by [84] and further developed in [9, 29]. Comparing Minkowski functionals to the S-parameters highlights the descriptive power of the three characterizing functions.

As expected, it is not possible to prove a one-to-one correspondence between the Minkowski functionals and most S parameters, that is one is not able to recover the exact S parameter values from the Minkowski functionals. However, it is often possible to show that both techniques basically catch the same information content. Also the S parameter set is heuristic, and which of both techniques offers better functional correlation has to be investigated by experiments.

- The amplitude parameters S_q, S_{ku}, S_{sk} and the "functional" parameters S_{bi}, S_{ci} and S_{vi} can be calculated from the Abbott curve, which is also one of the characterizing functions.

- Summit density S_{ds}: In section 3.2 it has been shown that Minkowski functionals can be linked to the Boolean grain model. If a surface's summits are modeled as grains, it is possible to estimate the summit density from the characterizing functions under the restriction of grain convexity[5]. The calculation of the parameter S_{ds} will surely yield differing results, but it can be expected that a correlation between both values can be observed. Unfortunately, the standard proposal [29] still does not include clearly defined algorithms, and a systematic investigation on real surface data has to be postponed. Although both methods aim for the same information, they work completely differently: While Minkowski functionals are a statistical technique, the calculation of S_{ds} is based on tesselation of the surface (cf. section 2).

- Arithmetic mean summit curvature S_{sc}: The same difficulty as for S_{ds} arises when comparing S_{sc} and Minkowski functionals. The latter can as well be used to describe the shape of peaks in terms of their typical area and contour length at a given level, and therefore some correlation between the latter and S_{sc} can be expected. Although this correspondence is admittedly vague, it indicates that a change in the S_{sc} might also be observable in the characterizing functions.

- Root mean square slope $S_{\Delta q}$: The estimation formula for the contour length (4.14) reveals that the integral over the contour length[6] is again

[5] For an experimental validation see section 5.4.

[6] This quantitiy also plays an important role in image processing, where it is known as the *total variation*[43].

very similar to the root mean square slope. The first is an integral (approximated in practice by a sum) over the absolute value of the gradient of the surface, while the latter is the square root of the sum of the squared gradients. Thus, the difference between both methods is the same as the difference between S_a and S_q: They will yield different values, but express a similar information content.

- Surface area ratio S_{dr}: As already noted in chapter 2, the surface area is such an intuitive and easy to calculate parameter that one would not think about replacing it. However, the surface area, which is the integral over the surface's normal vector, is very similar to the integral over the local gradient, which in turn is the integral over the contour length. Therefore, any functionality of the surface which can be related to the surface area is expected to be expressed also in the contour length.

The four remaining parameters S_z, S_{al}, S_{td} and S_{tdr} cannot be related to the characterizing functions. S_z is based on the geometrical decomposition of the surface, and the calculation concept behind it differs completely from the statistical approach of the Minkowski functionals. Therefore, a comparison is possible by using experimental or simulated data, but nothing can be said using theoretical results. However, in practice S_z and S_q often show an intimate relation[7]. S_{al}, S_{td} and S_{tdr} are related to the global behaviour of the autocorrelation function; Minkowski functionals only describe behavior of the autocorrelation functions at the origin, and non-local information will have less influence.

The above considerations indicate that a major part of the S-parameter set can be expressed or approximated by parameters derived from the characterizing functions. Actually, the S-parameters have in common that they are based on local properties of the surface[8]. This is also the limiting property of the Minkowski functionals: As Minkowski functionals are integrals over local curvature measures, they cannot be used to investigate large scale / long wavelength features. In the S parameter set, only the autocorrelation length, the texture aspect ratio and the texture direction involve non-local features. Thus, the Minkowski functionals together with the ACF can be considered as having at least the descriptive power of the S-parameter set.

These considerations further underline the usefulness of the Minkowski functionals for technical surface characterization.

[7] S_z is said to be around $6S_q$ as a rule of thumb, as $6S_q$ spans a range of approximately 99% of the amplitudes; this is similar to S_z, which is the difference between the highest peaks and lowest pits.

[8] Also Whitehouse [100] argues that local properties are the most important for surface characterization tasks.

4.1.4. Influence of noise

Before applying the proposed techniques in practice, it is important to investigate how the Minkowski functionals behave under the influence of measurement artifacts. Data sets only offer a distorted image of reality, as every measurement system induces artifacts such as outliers or homogeneous noise. If these artifacts are not removed by filters or implicitly in the feature calculation, the result might be misleading.

The effect of additive white noise is quity easy to understand: From linear systems theory it is well known that the autocorrelation function of white noise is a delta peak. Hence, additive white noise will only affect the ACF in the origin. Unfortunately, this is also the point that the evaluation of the Minkowski functionals is focused on: The variance of the data, which is the (unnormalized) ACF's value in 0, and the peakedness of the ACF in 0 are crucial factors for the shape of the characterizing functions. Thus, even low noise will have impact on the Minkowski functionals if the surface is smooth or has a small standard deviation. According to equation (3.3), adding noise to a GRF will stretch all three functions along the height axis by $\left(1+\sigma^2_{noise}/(2\sigma^2)\right)^{1/2}$. The contour length and Euler characteristic functions will be amplified by $\left(1+\sigma_{noise}/(|\tau|\sigma^2)\right)^{1/2}$ and $(1+\sigma^2_{noise}/(|\tau|\sigma^2))/(1+\sigma^2_{noise}/\sigma^2)^{1/2}$, respectively.

The effect of noise can also be understood when looking at the estimation formulae (4.16) and (4.20). Each term is based on first and second derivative estimated from local 3×3 environments. Adding noise amounts to increasing the variance in these neighbourhoods. Homogeneous noise will slightly increase the variance in all neighbourhoods, while single outliers strongly influence a small number of neighbourhoods. Accordingly, also the (expected) absolute values of first and second derivatives increase, the characterizing functions will be stretched, and the contour length and Euler characteristic will have a higher amplitude.

The conclusion of the above considerations is that noise can have a strong influence on the characterizing functions. Having in mind that Minkowski functionals are means over local properties of the surface, it is obvious that noise – which is a local phenomenon also – will have immediate impact, even if the large-scale properties of the surface are not affected by the noise. As a rule of thumb, the Minkowski functionals will best unravel their descriptive power if applied to denoised data. If the data is denoised by filtering first, each resulting pixel will contain information from a neighbourhood of pixels. Thus, the Minkowski functionals will not only describe the shortest wavelength, which contains most of the noise, but also the relevant microstructure.

4.2. Filtering and scale spaces

In technical surface characterization tasks, workpieces have to be analyzed separately on different scales as each scale is associated with specific functional properties. Friction, for example, will be influenced by small scale properties, whereas recasting would happen on the largest scales[9]. The need for scale separation has led to the the development of various filtering concepts for surfaces [88, 13, 93].

The application of a series of filters with varying bandwidths to the original data set, e.g. linear low-pass filters with increasing cutoff frequency, yields a series of smoothed data sets, the so-called scale space [40]. For each of these data sets, one can now calculate the characterizing functions. This leads to three families of real functions of the height of the level set and the filter parameters.

As pointed out in section 4.1.3, Minkowski functionals describe predominantly the smallest scale inherent in the data set. Thus, applying the characterizing functions to the scale space offers a possibility to investigate all scales of the image.

Scale spaces are widely used in image processing [32], and the filter techniques developed there can be adopted easily to surface microstructure characterization. In image processing, scale spaces are constructed by subsequently blurring the image. Finer structures will vanish and, accordingly, smaller scales will be removed from the data. The most important filters are linear filters and morphological filters, as described in the following.

4.2.1. Gaussian scale space

Linear filters [39, 32] blur the data by replacing each height value by the weighted sum of the height values inside a neighborhood. The weight matrix is denoted as filter mask. One of the most important filter types is the Gaussian filter. A Gaussian-shaped filter mask [13] results in a low pass filter which, roughly speaking, removes frequencies higher than a given cutoff wavelength. This cutoff wavelength depends on the width of the Gaussian used as the filter mask.

The effect of a linear filter on the characterizing functions can be understood most easily for realizations of Gaussian random fields. Here, the Minkowski functionals depend only on the autocorrelation function's behaviour at the origin. Using the Minkowski functionals, it is possible to

[9] The actual wavelengths of "small scale" and "large scale" depend on the resolution of the measurement device and the size of the measurement window; here, we assume to investigate scales ranging from μm to several mm; this is the scale of the data used in the context of this work, but is by no means universal.

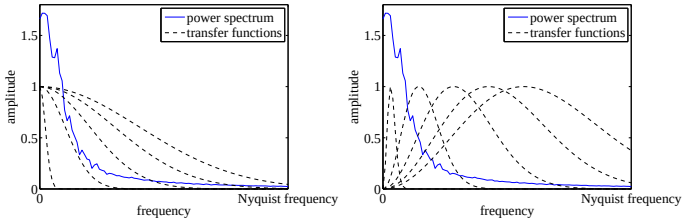

Figure 4.2.: Filter banks of Gaussian low pass filters (left) and band pass filters (right) for a typical sample spectrum. The maximal amplitudes of the band pass filter's transfer functions have been normed to 1.

estimate the filtered ACF's value at the origin (i.e. the variance of the surface) and their second derivatives' value at the origin. In the following, we assume that the data is filtered with a Gaussian low-pass filter.

The variance of the data set equals the integral over all frequency amplitudes in the power spectrum[10]. Applying a linear filter to the data yields a power spectrum multiplied with the power spectrum of the filter mask (the so-called transfer function). Thus, the variance of the filtered data is the integral over the weighted original power spectrum (figure 4.2).

As the ACF is the inverse Fourier transform of the power spectrum, the value of its second derivative for the filtered data is the result of the following operations on the power spectrum:

1. Multiplication with the transfer function.

2. Multiplication with $4\pi^2\omega^2$, where ω is the frequency, as the power spectrum of the ACF's derivative is the original power spectrum multiplied by a linear function with zero offset.

3. Integration over the whole frequency range, as the ACF's second derivative at the origin is the zero frequency in the power spectrums filtered by steps 1 and 2.

As sketched in figure 4.2, step 1 is a low pass filter; step 2 is a high pass filter, and the transfer function of the combination of both steps is a bandpass filter given by

$$4\pi^2\omega^2 \exp\left(-\omega^2/(2\sigma^2)\right), \tag{4.21}$$

[10] Here, only the one-dimensional case is considered. Since the random process used for modelling the data is assumed to be rotation-invariant, the results are valid also for the two-dimensional case.

where the frequency σ determines the shift of the pass band on the frequency axis.

These considerations show that the amplitude of the contour length and the Euler characteristic function of Gaussian filtered surfaces essentially depend on the surface's cumulated frequency amplitudes within a pass band. Vice versa, the spectrum can be reconstructed by evaluating the Minkowski functionals on a series of filtered data sets.

Linear filtering is most appropriate for surfaces which have a meaningful Fourier transform. For instance, the surface should not contain sharp edges and should not have a trend. Those surface are referred to as *statistical surfaces* in chapter 2. A typical example would be a shot-blasted surface (see also chapters 5 and 6), which has a homogeneous, statistical structure. For such surfaces, the Minkowski functionals calculated for filtered surfaces offer a possibility to characterize the different scales of the surface.

As argued in section 4.1.3, the Minkowski functionals cover the whole S-parameter set except for the information of the autocorrelation function. This is due to the restriction of the Minkowski functionals to the shortest scales in the surface. Using filtering, one can overcome this restriction by the description of lower frequencies.

4.2.2. Morphological scale space

Linear filters have the disadvantage that they blur edges or other sharp structures in the image. On the other hand, artifacts like outliers will never vanish completely in the filtered image. Therefore, morphological filters [81] have been introduced in image processing. The resulting scale spaces have been used widely in image processing to describe the content of gray-value images [51, 56]. The morphological operators can also be used to derive spezialized surface microstructure parameters, as detailed in chapter 6.

However, due to their nonlinearity, morphological operations are generally regarded as being hard to handle analytically. Luckily, this is not the case if morphological filters are used in combination with the boolean grain model and Minkowski functionals, as described in the following.

The dilation operator $\oplus$ on a gray value image $S : \mathbb{R}^2 \to \mathbb{R}$ is defined as

$$\begin{aligned} S^{(\text{filtered})} &= S \oplus B \\ S^{(\text{filtered})}(x) &= \max_{x' \in B+x} S(x'), \end{aligned} \tag{4.22}$$

where $B \subset \mathbb{R}^2$ is the so-called structuring element centered at the origin and $B + x$ denotes B shifted to the position x. That is, every gray value is replaced by the maximum of the gray values inside a neighborhood given

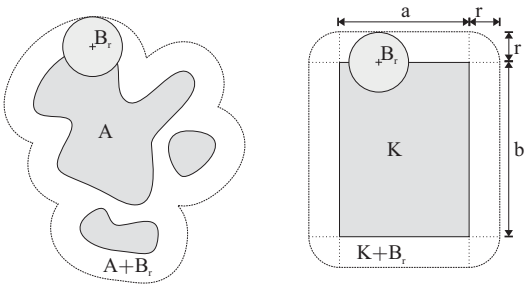

Figure 4.3.: Dilation of a set in $\mathbb{R}^2$. The right part of the figure demonstrates how Steiner's formula applies to a set with rectangular shape.

by B (see also figure 6.3). The dilation operator's effect can be compared to a low-pass filter: With increasing size of B, also larger structures will be removed by the maximum operator. For very large B, the filtered image will have the constant gray value $\max_{x \in \mathbb{R}^2} S(x)$. Although the structuring element B can be an arbitrary set, it is usually chosen convex. Important special cases are quadratic and disk-shaped structuring elements.

For a level set $A_S(h)$, this implies $A_{S \oplus B}(h) = A_S(h) + B$, where $+$ denotes the Minkowski addition $A+B = \{x+y, x \in A, y \in B\}$ of two sets $A, B \subset \mathbb{R}^2$, which is the well-known dilation operator for sets (figure 4.3).

Surprisingly, it is now possible to derive analytical formulae for the Minkowski functionals of dilations of sets. For the sake of simplicity and in accordance with the literature, the notations V_0, V_1 and V_2 are used for the Euler characteristic, contour length, and area, respectively[11]. Though the theory can be formulated for arbitrary dimensions, the following considerations are limited to $\mathbb{R}^2$.

Consider a given rectangular set K with length a and width b, which is dilated by a disk B_r with radius r. Then, the area of the dilated set is the area of the original set plus the area of two $r \times a$ and $r \times b$ rectangles plus four disk quadrants of a disk with radius r (fig. 4.3). The contour length is the contour length of the original set plus the disk perimeter, while the

[11] Note that V_i is an i-dimensional measure.

Euler characteristic remains constant. This yields

$$\begin{aligned} V_2(K+B_r) &= r^2\pi + 4r(a+b) + ab \\ V_1(K+B_r) &= 2r\pi + 2(a+b) \\ V_0(K+B_r) &= 1. \end{aligned} \tag{4.23}$$

This formula can be generalized to arbitrary convex sets $K \subset \mathbb{R}^2$, and one gets

$$V_n(K+B_r) = \sum_{i=0}^{n} r^{(n-i)} V_{n-i}(B_1) V_i(K), n \leq 2, \tag{4.24}$$

the so-called Steiner formula, one of the key tools in stochastic geometry. B_1 denotes the unit disk [76].

In the case of a boolean grain model with convex grains the level set A_S is the union of randomly positioned convex sets K_j. As

$$(K_i \cup K_j) + B_r = (K_i + B_r) \cup (K_j + B_r)$$

for $K_i, K_j \subset \mathbb{R}^2$, the dilation of the level set A_{S+B_r} is again a Boolean grain model with grains $K_i + B_r$. Therefore, according to (3.9),

$$\begin{aligned} V_2(A_{S+B_r}) &= 1 - \exp\left(-\rho\overline{V_2(K+B_r)}\right) = \\ &= 1 - \exp\left(-\rho \sum_{i=0}^{2} r^{(2-i)} V_{2-i}(B_1)\overline{V_i(K)}\right), \end{aligned} \tag{4.25}$$

where $\overline{V_i(\cdot)}$ denotes the expectation over the distribution of the grains K. In stochastic geometry literature, $V_2(A_{S+B_r})$ is usually referred to as the spherical contact distribution function, as it describes the probability that the ball B_r hits the level set if placed at a random position.

In practical applications the dilation of a height map with a disk-shaped structuring element can be problematic for disks with a small radius, as the approximation of a disk on a lattice will be quite coarse. Hence, eq. (4.25) will not coincide well with practical experiments. However, the above considerations can easily be extended to quadratic structuring elements, which harmonize better with data on a lattice. Replacing B_r with a $2r \times 2r$ square

C_r, (4.23) changes to

$$\begin{aligned} V_2(K + C_r) &= 4r^2 + 4r(a + b) + ab \\ V_1(K + C_r) &= 8r + 2(a + b) \\ V_0(K + C_r) &= 1. \end{aligned} \tag{4.26}$$

The corresponding Steiner formula becomes

$$V_n(K + C_r) = \sum_{i=0}^{n} r^{(n-i)} V_{n-i}(C_1) V_i(K), n \leq 2, \tag{4.27}$$

where C_1 is now a square with edge length 2. The change of the structuring element therefore only changes the constants of the polynomial.

The Steiner formula can also be used to calculate expressions for $V_0(A_{S+C_r})$ and $V_1(A_{S+C_r})$. The expressions are analogous to eq. (3.9) with the difference that area, contour length and Euler characteristic of the typical grain are replaced by the characteristics of the dilated grains. Vice versa, analyzing a dilated height map using formulae (3.9) means analyzing a Boolean grain model with dilated grains. This can be used for surfaces with rough grains, as demonstrated in section 5.4. Dilation of the height map means dilating the single grains, which is a smoothing operation. Although the original grains would not fulfill the convex grain assumption, the dilated grains become convex and the Boolean grain model analysis becomes feasible.

Using the results described above, one can develop analysis techniques beyond the scope of the original Minkowski functionals: The basic assumption for the validity of (4.26) is that the surface is based on a Boolean model. Hence, for a level set $A_S(h)$ at a fixed height h, the function[12]

$$\begin{aligned} \log\left(1 - V_2(K + C_r)\right) &= \log\left(1 - V_2(A_{S+C_r})\right) \\ &= -\rho \sum_{i=0}^{2} r^{(2-i)} V_{2-i}(C_1) \overline{V_i(K)} \end{aligned} \tag{4.28}$$

is always a polynomial of degree 2 in r. This can be used as a test for the validity of the Boolean grain model assumption [86].

One application could be a test for the homogeneity of a surface. The Boolean model stems from a Poisson process, that is from points distributed homogeneously in the measurement window. Therefore, if the surface is not homogeneous, for instance if the grains form clusters or leave sparsely

[12] It is possible to extend (4.28) to functions describing $V_0(K + C_r)$ and $V_1(K + C_r)$, but these yield less stable results in practical applications.

populated areas, this will affect the Minkowski functionals of the dilated images.

In practice (4.28) has to be treated with care. As argued above, problems can arise when the grains are not convex [28]; for large structuring elements, the argument of the logarithm approaches 0 and (4.28) will not be stable any more. Moreover, it turns out in practice (section 5.5) that quite large measurement windows would be necessary for a successful application of the described test.

5. Experimental results

5.1. Testing the estimators

To test and to compare the estimators proposed in section 4.1.2, simulation experiments were performed with GRF and Boolean grain models. These two models cover a wide range of possible surfaces. While GRF are usually smooth (depending on the chosen covariance function) and homogeneous, Boolean grain models contain sharp edges at the grain intersections. For both models, the exact expected values for the Minkowski functionals are known (eqs. (3.9) and (3.3)), and the mean of the estimator result for many realizations can be compared to the theoretically derived expected values.

From the simulations, the standard deviations of the Minkowski functionals can also be estimated. However, there are no easy-to-use analytical expressions for these standard deviations [55], and their analysis is limited to simulations.

In figure 5.1, one exemplary simulation result is given. The upper row shows the expected Minkowski functionals, the mean Minkowski functionals and their standard deviation calculated from 50 realizations. The lower row shows the deviation between expectation and the means obtained from the simulations. For a more complete understanding of the estimators' performance, the experiment has been repeated with various resolutions ($n = 50, 100, 250, 500$) of the simulation window for both the GRF and the Boolean grain model. The resulting plots are given in appendix A, figures A.1-A.6.

One general observation is that the GRF sampled on a 50×50 lattice is subsampled, that is the structures observed on finer lattices are not reproduced correctly. Accordingly, any estimator on this data set can be expected to fail.

Nevertheless, both Gray's estimator (section 4.1.2) and the estimator derived from integral geometry[1] (section 4.1.2) for the area fraction are very accurate for both the GRF and Boolean grain models. Especially for coarse lattices, the IG estimator yields a smaller bias. This can be explained by the relatively coarse approximation of the level set by pixels used in Gray's method. The IG estimator does not explicitly calculate level sets and can

[1] In the following, the latter is abbreviated by IG estimator.

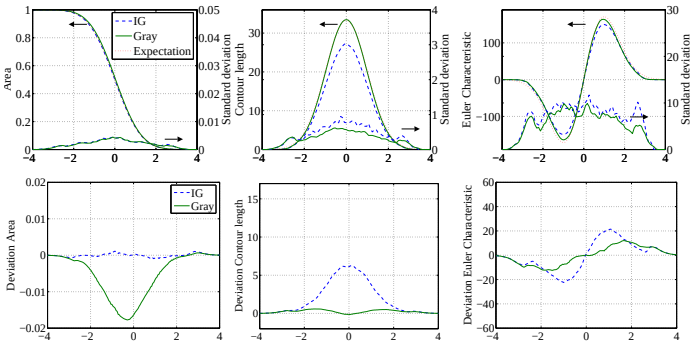

Figure 5.1.: Top: The expected and estimated characterizing functions and their standard deviation for 50 realizations of a Gaussian random field on a 100×100 lattice. Bottom: Deviation of IG and Gray's estimates from the expectation value.

thus achieve a better approximation. Considering the decrease of the bias towards higher resolutions[2], the estimator can be expected to be unbiased.

The situation is different for the contour length estimators. Here, for low resolutions, Gray's estimator yields a significantly lower bias. For higher resolutions, the IG estimator becomes superior. The lower performance of the IG estimator for low resolutions can be explained by its dependence on the first derivatives estimated from the image. The estimators of the first derivative using the usual $[-1\ 0\ 1]$ filter mask induces a smoothing of the data, which affects especially data which is sampled with a sampling rate below or close to the Nyquist frequency. Interestingly, Gray's estimator seems to get worse for higher resolutions. One remedy could be to change the factors in the weighted sum (4.2) depending on the resolution of the data.

On GRF realizations, the Euler characteristic is best estimated by Gray's algorithm independently of the resolution. Again, the estimation of the first derivative in the IG algorithm can be considered as the reason. On the Boolean grain model, Gray's algorithm slightly outperforms the IG algorithm for low resolutions. For high resolutions, Gray's algorithm is only better for high thresholds. Here, only few grains overlap and the Euler characteristic

[2] A mathematical proof of the (un)biasedness is beyond the scope of this thesis.

counts mainly isolated objects. This is done best by summing over local binary patterns.

The standard deviation of both estimators tends to a common curve for both estimators, where the limit seems to be approached already for relatively low resolutions. This indicates that the observed uncertainty is not a property of the estimator but is due to the variations of the simulations. This underlines the stability of both estimators.

The conclusion of the above considerations is that the area fraction function should always be estimated using the IG algorithm. If the resolution is low (i.e. the sampling rate is below or close to the highest significant frequency inherent in the data), Gray's algorithm is a more accurate estimator for the contour length. For large data sets, however, the IG algorithm is significantly faster. The same holds for estimation of the Euler characteristic. However, for high thresholds, Gray's algorithm can occasionally be more accurate.

In the following experiments, we use the IG algorithm, as it is more convenient for height maps consisting of up to 1000×1000 pixels.

5.2. Further simulation results

5.2.1. Gaussian random fields

In figure 5.2, the results for four other simulations are shown. The characterizing functions were calculated for Gaussian random fields with different covariance function shapes. All four GRF share the same distribution function, i.e. their material ratio function is the same. One observes also that the shapes of the contour length and Euler characteristic functions do not depend on the general shape of the covariance, but only on the value of its second derivative in 0, τ, as predicted by the analytically calculated functions (eq. 3.3). The differences in τ show up as different amplitudes of the characterizing function. Since the τ of the second (Gaussian-shaped covariance) and fourth (Bessel type covariance) GRF are the same, also their characterizing functions are almost identical[3]. Nevertheless, the realizations look different especially on longer scales. Accordingly, the characterizing functions cannot provide information on long-wavelength features of the surface. On the other hand, by means of a Taylor series, the covariance functions used can be approximated accurately by a parabola (this information is contained in

[3] In a perfect simulation, the characterizing functions would match exactly if τ was the same. However, as the circulant embedding algorithm [105] used to perform the simulations is only perfect for covariance functions with a finite support, deviations in the characterizing functions occur.

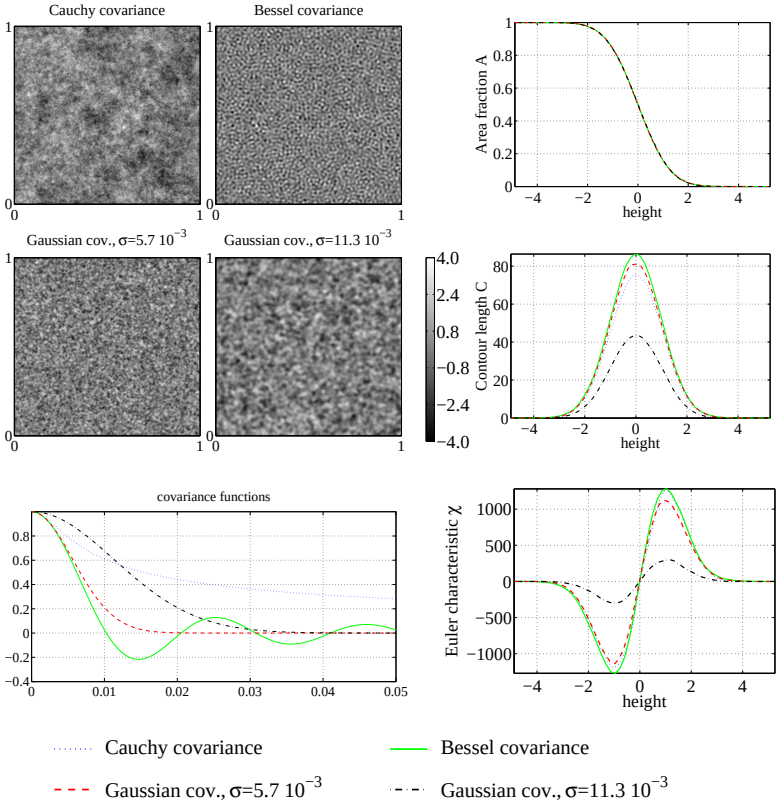

Figure 5.2.: Four realizations of Gaussian Random Fields (GRF) with same standard deviation $\sigma = 1$. All the GRF have the same material ratio function, but different covariance functions. The covariances of the first three GRF have the same parameter τ (the second derivative in 0).

the characterizing functions via the parameter τ) in the vicinity of 0. Regarding the roughness of a surface, these short-wavelength features are the information one is primarily interested in, as longer wavelengths would be identified with waviness or form and can be separated by a low-pass filter [83].

These results are valid also for the other random fields, and very similar simulation results can be obtained for these.

5.2.2. Markov random fields

For Markov random fields (MRFs), analytical expressions for the Minkowski functionals are not known and therefore, simulation results cannot be compared to analytical expressions as in the Gaussian random field (GRF) or Boolean grain model cases. However, some MRFs are special cases of GRFs, and their generalizations are still very similar to GRFs. Hence, comparing the Minkowski functionals of simulated MRFs with the analytical expressions for GRFs can reveal differences between the Minkowski functionals of both models.

In figure 5.3, four realizations of MRFs with a generalized Gaussian potential function (eq. (3.2)) are shown. The MRFs have been simulated on a 300×300 lattice using the Gibbs sampler [103] with the potential functions given by

$$V_{c_1,c_2}(s_{c_1}, s_{c_2}) = -b \left(\frac{s_{c_1} - s_{c_2}}{\sigma_V} \right)^p, 0 < p.$$

with $b = 2$, $\sigma_V = 1$ and $p = 0.6, 1.2, 2, 3$, respecively. The MRF with $p = 2$ is also a GRF.

The mean characterizing functions for 10 realizations each of the MRFs with $p = 0.6, 1.2, 2, 3$ are plotted in figure 5.4. Furthermore an analytical characterizing function of a GRF has been fitted (cf. section 5.3) to each of the mean characterizing functions. The deviation between the best fit and the mean of the simulation is plotted in figure 5.5.

Investigation of these deviations reveals that the area fraction function, that is the marginal distribution of the MRFs, is very close to that of a Gaussian. The deviation between the estimated area fraction and the expected area fraction of a GRF is small enough to be explained by simulation and estimation errors. Also the contour length and Euler characteristic functions basically look like in the case of GRFs (fig. 5.4), and it is possible to fit a GRF's expected contour length or Euler characteristic function if the other characterizing functions are disregarded. However it is not possible to satisfactorily fit all three expected characterizing function simultaneously (fig. 5.5). This is not even possible for the simulation with $p = 2$, which should

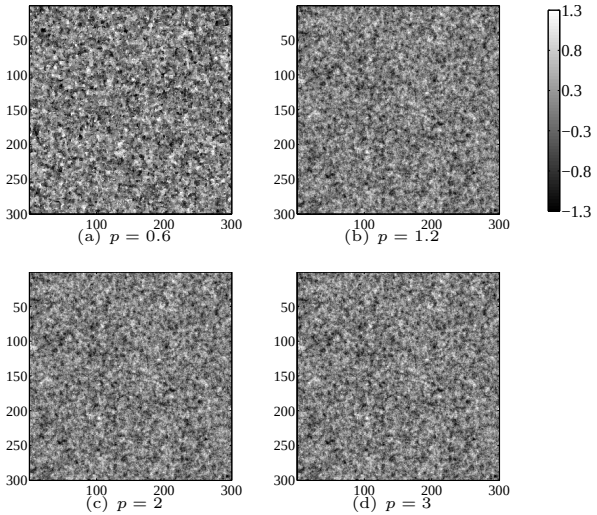

Figure 5.3.: Realizations of MRFs with generalized Gaussian potential functions with parameters $b = 2$, $\sigma_V = 1$ and $p = 0.6, 1.2, 2, 3$.

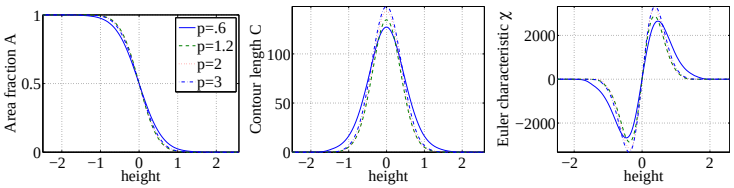

Figure 5.4.: Summarized characterizing functions for 10 realizations of the MRF depicted in figure 5.3.

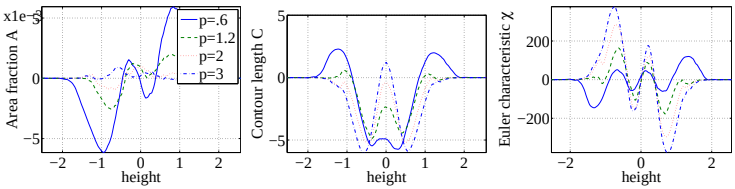

Figure 5.5.: Deviations between the characterizing functions estimated from simulations and the analytically calculated characterizing functions of GRFs fitted to the latter.

actually be a GRF. The deviation can therefore be explained by insufficiently accurate simulations.

However, instead of comparing the characterizing functions over the whole threshold height range, a simplified test is possible. As known from the analytical expressions for the characterizing functions of GRFs, these depend only on the standard deviation σ of the GRF and the second derivative τ of its autocorrelation function. Precisely, the maximal amplitude of the contour length C_{max} depends on $c_1\sqrt{\tau}$ and the maximal amplitude of the Euler characteristic χ_{max} on $c_2\tau$ with constants $c_1, c_2 \in \mathbb{R}$. Therefore, plotting χ_{max} versus C_{max} for GRFs with varying τ yields a parabola with a small curvature (fig. 5.6), denoted by f_G in the following.

In figure 5.6, χ_{max} versus C_{max} is also plotted for the MRF simulations. The data can be approximated by a straight line or a parabola with small curvature, denoted by f_M. Here, f_G and f_M intersect for $p \approx 2$, since the MRF is a GRF for $p = 2$. Interestingly, the two functions do not coincide for $p \neq 2$. That is, the MRFs' characterizing functions actually do differ from GRF's characterizing functions as the relation between their contour length's amplitude and their Euler characteristic's amplitude is in general different from the GRF case. This relation depends on the shape of the potential function of the MRF.

These experiments show that even if the data's amplitude distribution is Gaussian, the data is not necessarily a realization of a GRF. Comparing the characterizing functions estimated from data to the characterizing functions of a GRF can reveal the non-Gaussianity of a surface.

5.2.3. Boolean grain models

The last simulation example shows two Boolean models. The grains of the first boolean model have been chosen to be cylinders of random height with

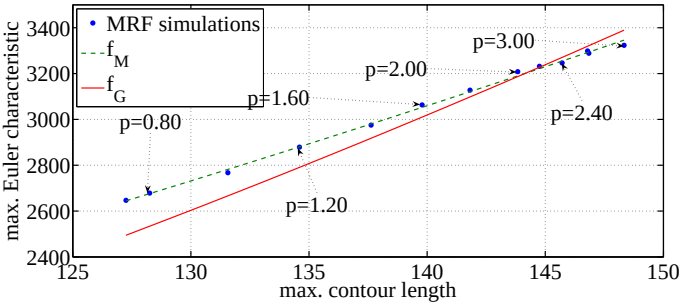

Figure 5.6.: Maximum of the Euler characteristic function plotted versus the maximum of the contour length function for the characterizing functions of MRF and the expected characterizing functions of GRF. f_M and f_G coincide for $p = 2$, for which the MRF is also a GRF.

spherical caps and constant diameter (fig. 5.7, upper left). In the second model, the void area is modeled and the grains are troughs with a triangular-shaped cross section (fig. 5.7, bottom left). The location and orientation of the troughs is random, but their shape is fixed.

Again, the expected and measured characterizing functions are compared, calculated for 50 realizations with a resolution of 500×500 pixels.

For high thresholds, both estimators are very accurate and analytically calculated and simulated characterizing functions coincide; for low thresholds, the estimators for the trough model become unstable and the calculated contour length and Euler characteristic show a large deviation from their expected values (dashed lines). This can be explained by aliasing effects: In the level sets, sections through the troughs appear as bars, which become narrower as the cutting level is decreased. Finally, the lines become so thin that they cannot be resolved by the chosen pixel resolution. The lines break up into several shorter segments. This causes the formerly connected line-shaped void areas to appear as many small isolated void areas. Thus, the Euler characteristic suddenly falls below zero and shows a large deviation from the expected value. The aliasing effect can be reduced by increasing the sampling rate but will never vanish completely.

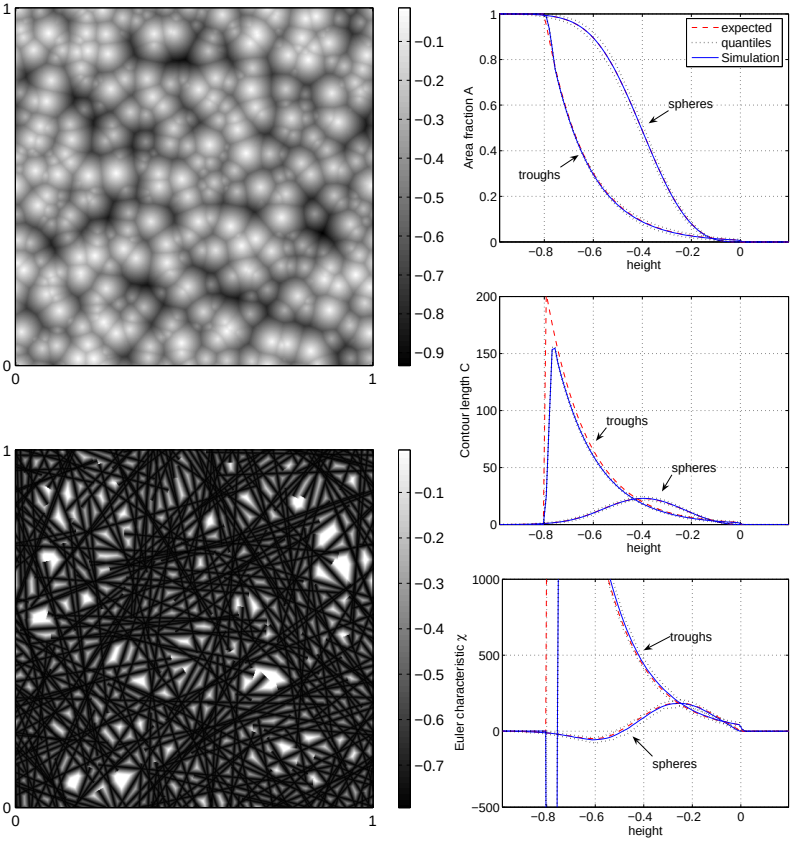

Figure 5.7.: Two realizations of Boolean models and the summarized characteristics of 50 realizations each.

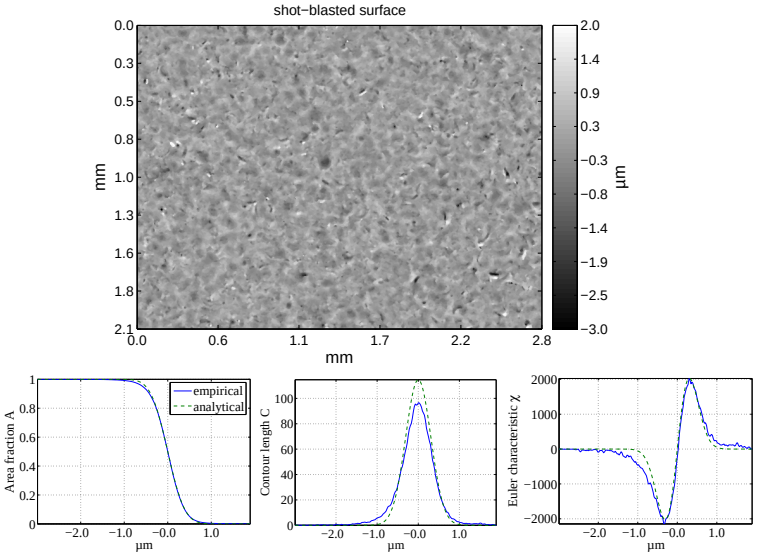

Figure 5.8.: A measurement of a shot-blasted surface and the empirical and fitted analytical characterizing functions.

5.3. Experiments on shot-blasted surfaces

The shot-blasted surfaces were measured with a NewView Delta white light interferometer (Zygo, Middlefield). The surface (fig. 5.8) does not show any regular texture. It looks purely random and is therefore likely to match the random field assumption.

Before calculating the characterizing functions, it is necessary to apply a preprocessing filter step. Especially outliers cause high frequencies in the data's Fourier spectrum. As Minkowski functionals tend to concentrate on these high frequencies[4], one would basically describe the noise if applying the characterizing functions to the unfiltered data. A suitable filter to remove outliers is the 3×3 median filter which replaces a height value by the median of the height values in a 3×3 environment. As the filter mask size is small in comparison with the observed extent of the typical microscopic structure, it does not oversmooth and retains the surface structure.

In figure 5.8, the empirical characterizing functions for the filtered surface are plotted. Analytical expected functions for GRF were fitted using a weighted least squares minimization according to eq. 3.3. The deviations between empirical and analytical functions were weighted proportional to the empirical probability density function[5]. Thus, deviations between the functions for high and low thresholds contribute less to the error than deviations in the core part of the surface.

As in the Markov random field example, it is possible to independently fit characterizing functions to the contour length function and the Euler characteristic functions such that the fitted functions show almost perfect coincidence of the fitted and empirical functions in the core part of the surface.

Yet the functions' tails cannot be matched exactly; the deviations are higher than those typically observed in simulations (fig. 5.1). Moreover, contour length and Euler characteristic cannot be fitted simultaneously. The estimated distribution of the height increments in neighboring pixel pairs – from equations (4.14,4.17) and [89] it is known that the contour length and Euler characteristic depend on the distribution of the increments – reveals that this distribution is not Gaussian, as it would be required for a surface to be a realization of a Gaussian random field. Instead, the distribution's tails are heavier than a Gaussian's. Hence, the surface is in general smooth, but contains also sharp edges. These sharp edges result in high increments, which

[4] High frequencies are related to the behavior of the autocorrelation function (ACF) close to the origin. The characterizing functions are again related to the ACF behavior at the origin, see section 3.2.4

[5] Weighted least squares methods are common in robust statistics, where one tries to reduce the influence of less reliable data.

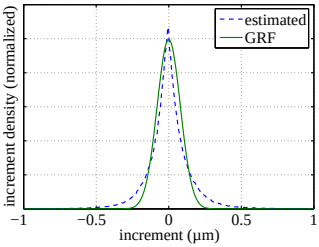

Figure 5.9.: Increment distributions of the shotblasted surface data and a Gaussian random field.

in turn influence contour length and Euler characteristic in the observed way.

As the data is not a realization of a Gaussian random field, it is not straightforward how the width of the estimated height probability density – this parameter is the most basic parameter to describe surface roughness – should be calculated. The usual approach is to simply estimate the data's standard deviation, which yields the surface roughness parameter S_q. Alternatively, it is possible to fit a Gaussian distribution function to the material ratio function (fig. 5.8). The first approach yields $\sigma = 0.344\mu m \pm .009\mu m$[6], the second $\sigma = 0.310\mu m \pm .005\mu m$, which is significantly smaller. The reason is that the fit to the characterizing functions focuses on the core part of the surface while the heavier-than-normal tails are almost neglected.

It has to be emphasized that none of the two methods can be regarded as 'superior'; as the surface is not perfectly Gaussian, it is a matter of choice how the Gaussian model is fitted to the data. Nevertheless, the fit using the characterizing functions is more robust as outliers, which will only contribute to high and low levels' Minkowski functionals, will have only a small influence on the estimated parameters.

Similarly to the standard deviation estimation, also the estimation of τ, the autocorrelation's second derivative in 0, from the shot-blasted surface data yields significantly different results when estimated from the characterizing functions ($\tau = -0.111 \pm .002$) or from the empirical ACF ($\tau = -.100 \pm .002$). A similar effect can be reproduced in simulations if salt-and-pepper noise is added to the simulation. The estimator for $|\tau|$ based on the characterizing functions is more susceptible to noise than the estimate derived from the empirical ACF. This behavior is plausible: The noise is

[6] The confidence intervals were estimated by shifting a window of half the height map size over the height map and calculating the Minkowski functionals for each of the windows.

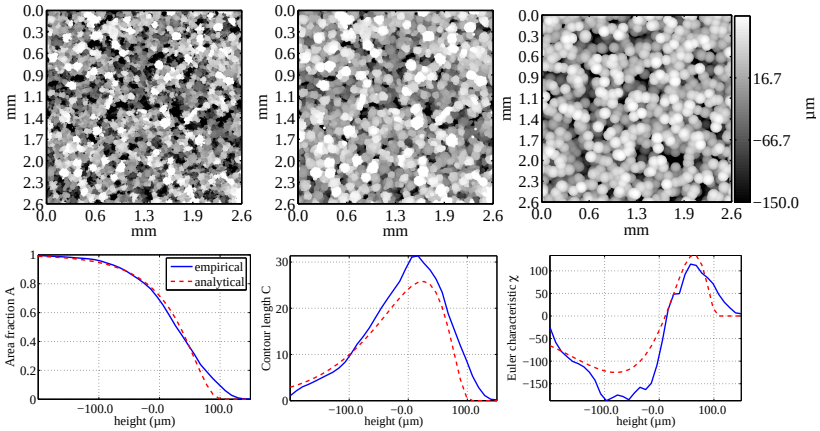

Figure 5.10.: Original, preprocessed and simulated surface of a sinter material and the characterizing functions for the preprocessed and simulated data.

sparse in relation to the remaining data points and will not have a large impact on the empirical autocorrelation. In contrast, the estimator based on the characterizing function is related to the amplitude of the contour length function which reaches its maximum at threshold $h = 0$. The contour length of the level set at threshold 0 will be considerably higher due to small "holes" and "needles" induced by the noise. The same argument applies to the measurement data, which contains sharp edges. These cause the contour length to become large enough to explain the observed deviation.

As in the following example, the effect described above stresses the importance of a proper preprocessing, which can have significant influence on the results obtained.

5.4. Experiments on sinter material

The sinter material under investigation consists of metal grains which have been fused in a thermal process to form a solid material. A KORAD S18 white light interferometer (3D-Shape, Erlangen) was used to acquire a 1000×1000 height map of the material surface. Neglecting the effect that

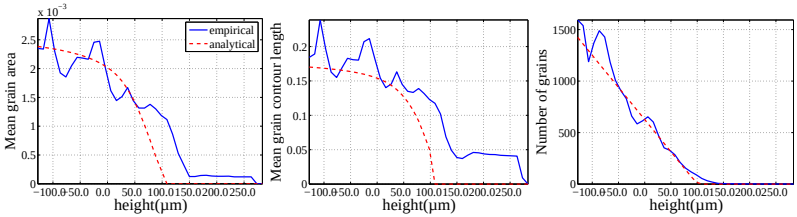

Figure 5.11.: The mean grain characteristics $\bar{A}$, $\bar{C}$ and $\rho\bar{\chi}$ calculated from the estimated characterizing functions

these grains can only overlap partially in reality, the material structure can be modeled with a boolean grain model. The grains in the model can be assumed to be cylinders with spherical caps, since a grain appears as a cylinder when viewed from above. The cylinders' radius and height are both assumed to be uniformly randomly distributed on a fixed interval.

A measurement of such a surface is depicted in figure 5.10. A closer look reveals that the single grains are not exactly convex. Since the surface is modeled using cylinders, one has to make the grains more convex. Therefore, a gray-value dilation with a disk-shaped structuring element of radius 6 is applied to the original data. As a consequence, the single grains get slightly larger[7]. In practice, one has to take care not to dilate too much, as the estimators will get unstable if the area fraction approaches 1. Additionally, a 3×3 median filter was applied before the dilation step to remove outliers, since dilating outliers would produce small grain-like artifacts.

Now the characterizing functions can be estimated from the data and the model parameters can be chosen such that the expected characterizing functions (eq. 3.9) best fit the empirical ones (fig. 5.10)[8]. The fit can be calculated using a least mean square error approach. Although a perfect fit to the empirical characterizing functions is not possible, the model parameters can be chosen in a way to catch the most important features. A simulation with the estimated parameters produces a height map very similar to the real data (fig. 5.10).

Although the simulated surface (fig. 5.10) looks convincing, the deviations between the estimated and the fitted characterizing functions have to be ex-

[7] Dilations in the context of random sets lead to so called contact distributions, an important tool for the analysis of boolean models. For details, see e.g. [55].

[8] The derivation of explicit analytic expressions for $\bar{A}$, $\bar{C}$ and $\bar{\chi}$ in eq. 3.9 is only practical for very simple models. Instead, numeric integration was used to calculate the expected Minkowski functionals for the model parameters.

plained. For a better understanding, the equation system 3.9 is solved for $\bar{A}(u)$, $\bar{C}(u)$ and $\rho\bar{\chi}(u)$. The resulting functions are shown in figure 5.11. In the transformed functions, the deviations look considerably different. First, one observes that the assumption of uniform distributed heights of the grains is only tenable for the core part of the surface, where $\rho\bar{\chi}(u)$ can be approximated by a straight line. For large thresholds h, where the model assumes no grains, a few grains still exist in practice (see also fig. 5.10). This also explains that the expected mean grain area and mean grain contour length functions do not follow the estimated functions for large h. Second, the expected grain contour length function lies below the estimated[9]. This is due to the fact that even with the dilation used as preprocessing, the grains in the measurement are still not exactly convex; therefore, the observed mean grain contour length is higher than expected from a convex grain.

These findings show that within the context of a specific model (e.g. boolean grains), it is possible to compute adjunct descriptors (e.g. $\bar{A}$, $\bar{C}$ and $\bar{\chi}$) that capture the entire information content, and are more directly interpretable in terms of that model (e.g. as describing grain shape).

5.5. Experiments on structured hard chrome surfaces

The last surface under investigation is a structured hard chrome surface (fig. 5.12). The surface consists of hemispheres which have been applied to a flat substrate in a galvanic growing process. The hemispheres have random radii and are positioned randomly, where an overlap of neighboring hemispheres is possible. Application areas of such surfaces are the structuring of sheet metal or the interior coating of transport pipes [90].

This coating is a good example for "designer surfaces", which are expected to gain great importance in the near future, as they allow to specifically design surface features optimized to fit the needs of a given application. The surface furthermore perfectly harmonizes with the analysis techniques proposed in chapter 3, as it ideally matches the Boolean grain model: The centers of the hemispheres can be assumed to be fixed on a plain defined by the underlying substrate – this assumption is motivated by the galvanic growth process producing the chrome hemispheres–, whereas the grain radii are assumed to be distributed according to a Gaussian distribution modified such that grains with negative radii are not allowed.

Three samples have been measured with a Zygo Delta white light interferometer (Zygo, Middlefield) with a 10× magnification, yielding a pixel size of $0.56\mu m$ (fig. 5.12). Two samples are homogeneous, whereas in the third

[9] The parameters of the model using circular grains cannot be chosen such that both mean grain area and mean grain contour match the estimated values

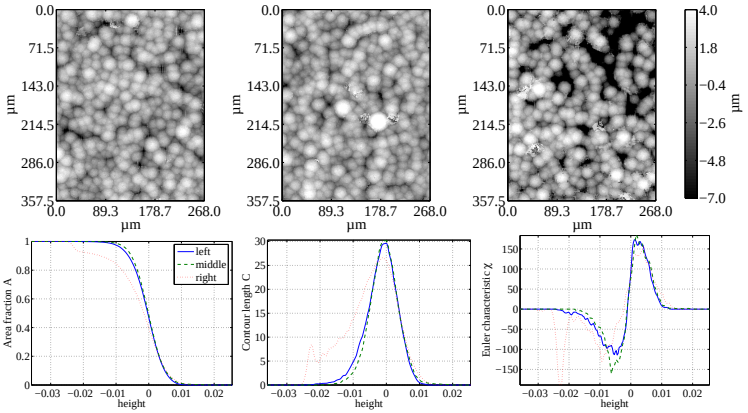

Figure 5.12.: Three measurement samples of structured hard chrome surfaces and the characterizing functions calculated from the filtered samples.

measurement, the grain positions are nonuniformly distributed. In practice, the measurements are partly corrupted by measurement artifacts like outliers or noise. Furthermore, the chrome hemispheres are not perfect hemispheres but slightly structured. Hence, all measurements have been preprocessed with a 7×7 median filter to assure a smooth surface.

Just like in the sinter material example, a Boolean grain model can be fitted to the data by means of the characterizing functions (fig. 5.13). Due to the high quality of the measurement data, the fit is almost perfect. Futhermore the structured chrome surface matches the Boolean grain assumption better than the sinter material, as the hemispheres are positioned independently of each other and are smoother than the sinter grains.

The above results show that it is possible, for given characterizing functions, to choose the Boolean grain model's parameters such that the expected Minkowski functionals exactly fit the given characterizing functions. This can be used effectively for a systematic surface engineering, as the Boolean grain models' parameters – these coincide with the manufacturing process parameters in the structured chrome example – can be determined such that the resulting surface has the demanded features. Furthermore, it can be decided early if it is possible to exhibit specific features and thus, the proposed technique can be used to show up limits set by the manufacturing process.

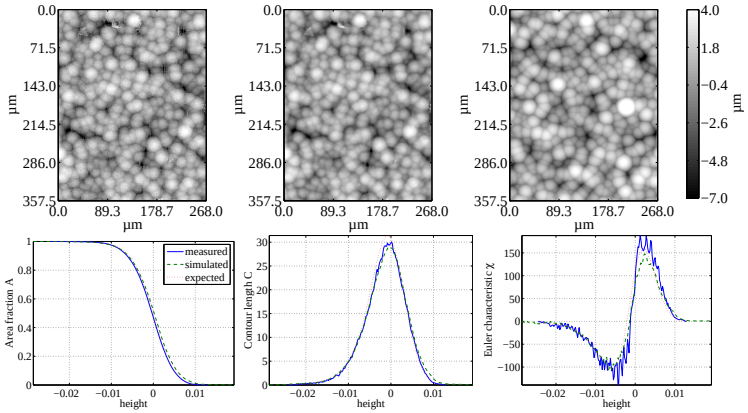

Figure 5.13.: Original, preprocessed and simulated surface of a structured chrome surface and the characterizing functions for the preprocessed and simulated data.

The advantage is that this can be done effectively without actually having to simulate or even to manufacture surfaces.

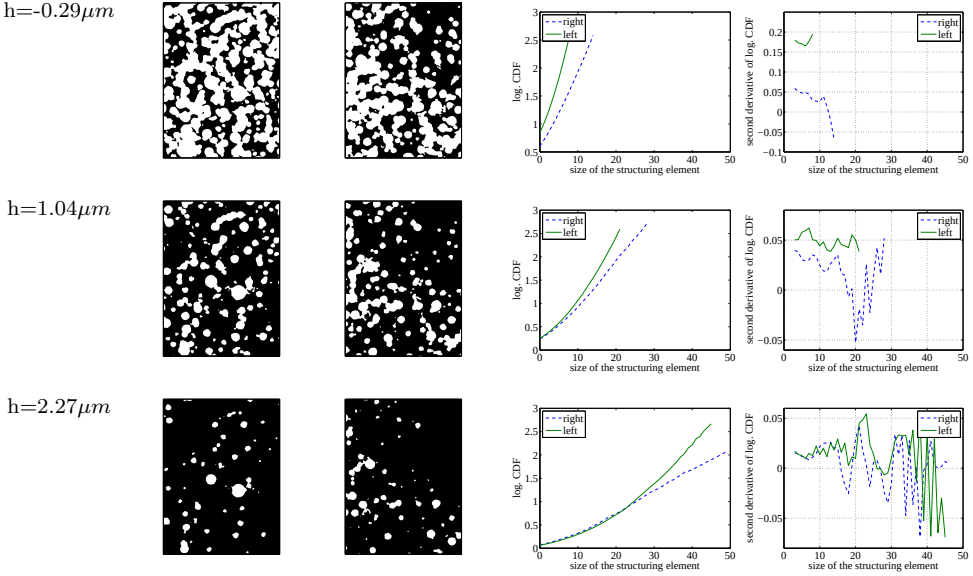

Figure 5.14.: Level sets and logarithmic contact distribution functions at thresholds $h = -0.29\mu m$, $1.04\mu m$ and $2.27\mu m$ for two of the structured hard chrome surface shown in figure 5.12.

In section 4.2.2 it has been shown that if a surface is a realization of a Boolean grain model, the logarithmic contact distribution function – i.e. the area fraction of dilated level sets as a function of the size of a structuring element – has a parabolic shape with positive curvature. This behavior has been proposed as a test for the homogeneity of spatial point patterns [6, 49, 91], and might be used as a test for the homogeneity of a surface.

One of the samples shown in figure 5.12 is inhomogeneous in the sense that a part of the sampling window is only populated sparsely by grains. This is also visible in the level sets (fig. 5.14). For both homogeneous and inhomogeneous surfaces, the logarithmic contact distribution functions have been computed (fig. 5.14). According to equation (4.28), the logarithmic contact distribution functions are parabolas for a perfect Boolean grain model.

The logarithmic contact distribution functions for the lower two level sets of the homogeneous surface are actually parabolic, that is their second derivative is approximately constant for small structuring elements; for large structuring elements, the logarithmic contrast distribution functions becomes unstable. In contrast, the corresponding logarithmic contact distribution functions for the inhomogeneous surface have a more complicated shape. Especially the parts of the function with a negative curvature are of interest. The curvature becomes negative if most of the level set is filled by the preceding dilations, but some large empty areas still persist. In this case, the increase of the logarithmic contact distribution function slows down, an indicator that the level set is not homogeneous.

For the highest level set this behavior is observable for both surfaces, although it is more distinctive for the inhomogeneous surface. Yet, a closer look of the level set of the homogeneous surface reveals that it is not perfectly homogeneous, as there are only a few grains in the upper left corner. In this case, a larger measurement window would be helpful to acquire a more robust statistics.

This experiment shows that calculating the contact distribution function or, generally, the Minkowski functionals of dilated surfaces, can be used to gather detailed information about the structure of a surface beyond the estimation of model characteristics. The proposed technique is most useful if some prior knowledge about the surface, e.g. the number of grains, is available. In this case, the expected contact distribution function can be compared to the contact distribution function estimated from the data, revealing differences between the measured surface and its modeled counterpart.

6. A three-dimensional measure of surface roughness

In chapter 4, morphological filters have been introduced to extend the capabilites of the characterizing functions. In the following, a further application of mathematical morphology to technical surface data is proposed.

While theoretical advances towards a characterization of 3D surface texture have been made [84, 9], culminating in a proposal for a new ISO standard for 3D surface characterization [29], in practice the evaluation of the acquired data is often still based on the parameters developed for tactile 2D-measuring instruments: even if a complete 3D data set is available, roughness characteristics are calculated from a set of intersecting or parallel 2D line segments.[1]

When it comes to specifying the roughness of technical surfaces, R_z and R_a are the most common choices [88]. R_a is the mean absolute deviation from zero of the high-pass filtered profile (figure 6.1). R_z is defined as [31]

$$R_z = \frac{\sum_{i=1}^{5} R_{z_i}}{5}. \tag{6.1}$$

R_{z_i} are the vertical distances between the highest peak and the lowest valley in each of five consecutive line segments l_r of a high-pass filtered profile. Accordingly, R_z is an extreme value statistic which summarizes extreme valleys and peaks (figure 6.2).

Obviously, the methods developed for 2D profiles do not fully exploit the information available in a 3D measurement, and new areal descriptors should be used.

Recently, a new standard for areal surface texture characterization has been proposed [29], which offers a replacement of the old R_z by S_z^{10}. S_z^{10} is the ten point height of the surface, expressing the difference between the ten highest peaks and ten lowest pits on the filtered surface. In contrast to R_z (fig. 6.2), which simply evaluates maxima and minima on the distinct line segments, S_z^{10} is based on peaks and pits which can be located anywhere on the surface. The extraction of the relevant peaks and pits is not an easy task [78], but can be accomplished with advanced computing techniques [29, 104].

[1] Unfortunately, the extraction of a profile segment itself from a matrix of height values requires interpolation if the sampling points of the line do not match the grid given by the matrix, which will yield a distorted profile.

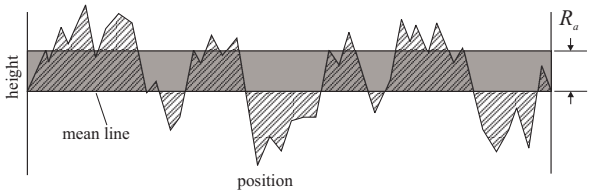

Figure 6.1.: Calculation of the profile roughness parameter R_a. The hatched area under the curve equals the area of the gray rectangle.

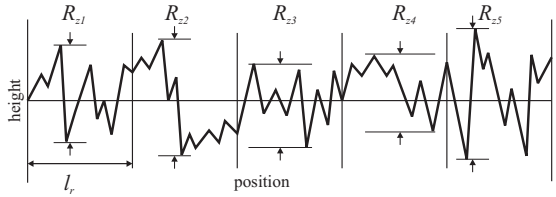

Figure 6.2.: Calculation of the profile roughness parameter R_z.

S_z^{10} generalizes the definition of an extreme value characteristic based on the five highest peaks and five lowest pits of a roughness profile. As such, it is susceptible to outliers.

6.1. A Generalization of R_z to 3D

The first step towards a generalization of R_z is to drop the requirement of non-overlapping line segments. Instead, the line segment l_r can be shifted over the whole profile. Similar to eq. 6.1 the vertical distance between the highest peak and the lowest valley on the line segment l_r shifted by i sampling points is denoted as R'_{z_i}. If l_r consists of M measured amplitudes from a total of N amplitudes $p_1, \ldots, p_N$ which are spaced with $\delta = \frac{l_r}{M-1}$, this yields

$$R'_{z_i} = \max\{p_{i+1}, \ldots, p_{i+M}\} - \min\{p_{i+1}, \ldots, p_{i+M}\}. \tag{6.2}$$

R'_z then can be defined as the mean over all R'_{z_i}:

$$R'_z = \frac{\sum_{i=0}^{N-M} R'_{z_i}}{N - M + 1}. \tag{6.3}$$

Now it is not a big step to generalize R_z further. When moving from a 2D measurement to a 3D measurement, averages analogous to eq. 6.3 can be calculated by shifting the line segment not only along the profile, but over the whole measurement area. However, the calculation of R'_{z_i} from amplitudes along a line segment is no longer adequate. If the surface is non-isotropic, the outcome of eq. 6.3 strongly depends on the direction of the segment. It is possible either to take the mean over all directions, in which case it is necessary to interpolate the data on the grid or, better, to choose a support for R'_{z_i} which does not emphasize a certain direction. The most isotropic generalization of a 1D line segment to 2D is a disc, and therefore R'_{z_i} in eq. 6.3 is replaced by $S_{z_{kl}}$, the vertical distance between the highest peak and the lowest valley on a disc of radius r located at grid position kl.

The formula corresponding to eq. 6.3 for an $N \times M$ height map becomes

$$S_z^{morph} = \frac{1}{(N - 2r)(M - 2r)} \sum_{k=r+1}^{N-r} \sum_{l=r+1}^{M-r} S_{z_{kl}} \tag{6.4}$$

To compute S_z^{morph} according to eq. 6.4, for each grid point of the height map, the maximum and the minimum amplitude in the disc centered on that

grid point have to be found. Then, the two resulting matrices are subtracted and the mean over all values is taken, which gives S_z^{morph}.

The original R_z can yield different values depending on the direction of the underlying line segment. Since S_z^{morph} is based on a rotation-invariant structuring element, it is not influenced by surface texture directionality and can thus be applied to surfaces with and without directional texture. On the other hand, it is not possible to investigate surface texture directionality using S_z^{morph}.

The task of finding local minima and maxima can be implemented by means of the well-known dilation and erosion operators from morphologic image processing [81], using a disc-shaped "structuring element" if radius r (figure 6.3). The difference between the dilated and the eroded images is called *morphological gradient* [32]; accordingly, S_z^{morph} as defined in eq. 6.4 is denoted as *morphological* S_z.

Thus a surface roughness parameter has been related to an established morphological image operator that is available in many image processing packages.

S_z^{morph} is closely related to the volume scale function S_{vs} defined in [29, 15]: The volume scale function is the volume between a morphological closing and opening of the surface using square structuring elements of various sizes (figure 6.4). Except for the shape of the structuring element, S_z^{morph} is nothing but the value of S_{vs} at a given scale, divided by the evaluation area. A difference is that the proposed standard [29] suggests evaluating the derivative of the volume scale function S_{vs} with respect to the the scale, whereas the above derivation of S_z^{morph} reveals that the absolute value of the related S_z^{morph} is also informative.

The plausibility of this connection is underlined by the use of morphological filters to calculate the upper and lower envelope of a surface [30]. Morphological filter operations similar to those mentioned above have been used to compute envelopes for the analysis of surface roughness [19]. Other applications are the extraction of topological features [79], thus making mathematical morphology an important tool for the analysis of surface data.

6.2. Experimental setup

To evaluate the performance of the S_z^{morph} defined above, measurements of different technical surfaces were acquired. Ground and two kinds of shot-blasted surfaces (specimen R1 to R7, R8 to R14 and R15 to R20, respectively) with different process parameters (figure 6.5) were compared; the specimens were characterized using a tactile device (Mahr Perthome-

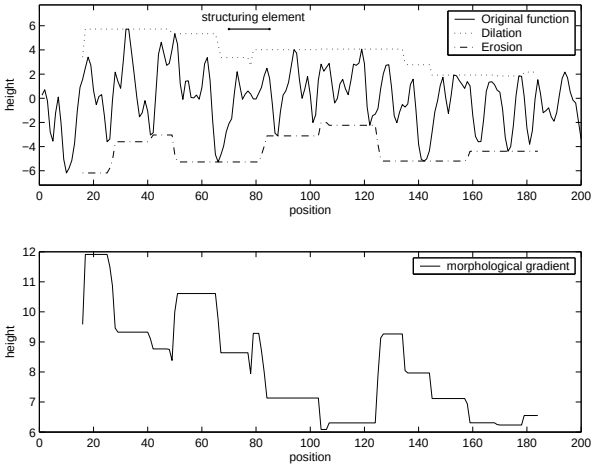

Figure 6.3.: Dilation and erosion of a 2D-function with a given structuring element (top) and the morphological gradient calculated from these (bottom). The spatial average of the morphological gradient gives the surface roughness estimate R'_z, see eq. 6.3.

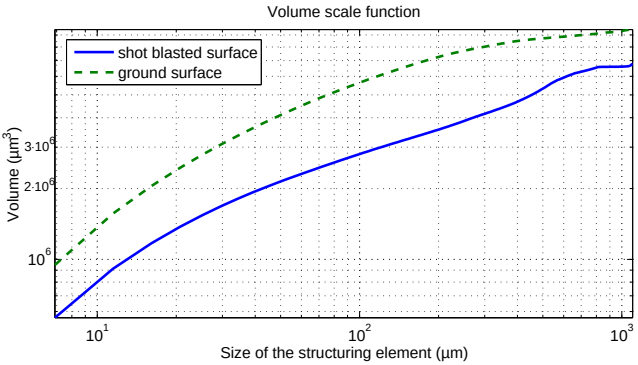

Figure 6.4.: Volume scale function S_{vs} of ground and shot-blasted surfaces (cf. fig. 6.5). S_{vs} is the volume between a dilation and an erosion of the surface; S_{vs} is plotted as a log-log plot.

ter, Göttingen), and a white light interferometer with a pixel resolution of 2.3μm (Zygo NewView 5000, Middlefield). This pixel resolution was chosen to match the size of the stylus tip of the tactile device. On each specimen, four different regions were measured. Tactile and optical measurements were performed at the same locations on the specimen so that the results could be directly compared.

On the acquired data sets, the following parameters were calculated:

- the tactile R_z according to [31] with a cutoff wavelength of 0.8mm, using $l_r = 0.8mm$
- S_z^X, the average over the R_z values in each line of the height map, which was calculated by Zygo's Metropro software [108]
- the S_z^{morph} defined in eq. 6.4

All optical measurements were filtered with a 3D-Gaussian filter with cut-off wavelength 0.8mm in vertical and horizontal direction.

The shot-blasted surfaces were non-directional. The ground surfaces did exhibit scratches, but these did not show a preferred directionality. Therefore, not only S_z^{morph}, which ignores the surface texture direction by definition, but also R_z and S_z^X are approximately independent of the rotation of the surfaces.

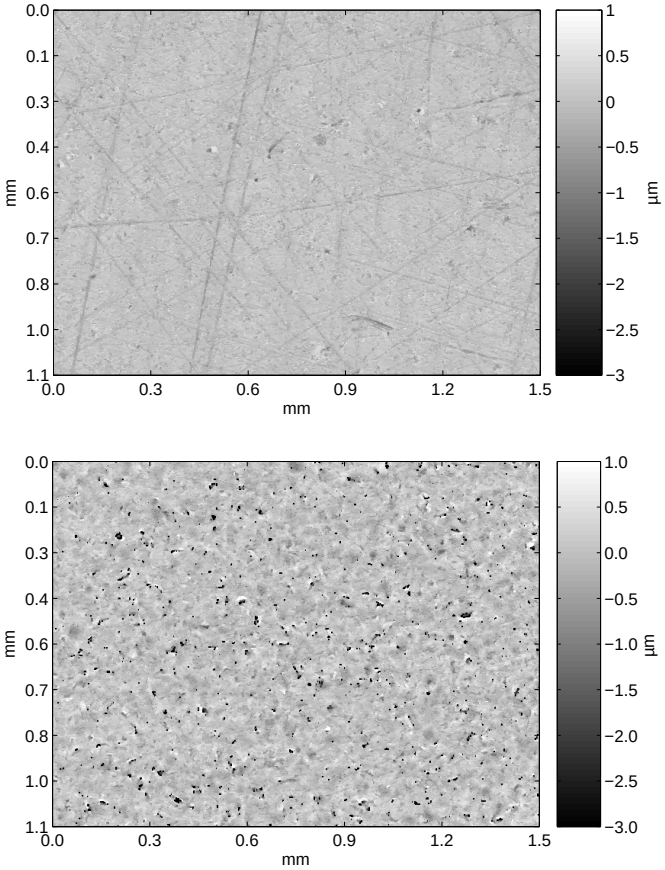

Figure 6.5.: Height maps of a ground and a shot-blasted surface used in the experiments. Black pixels denote missing data.

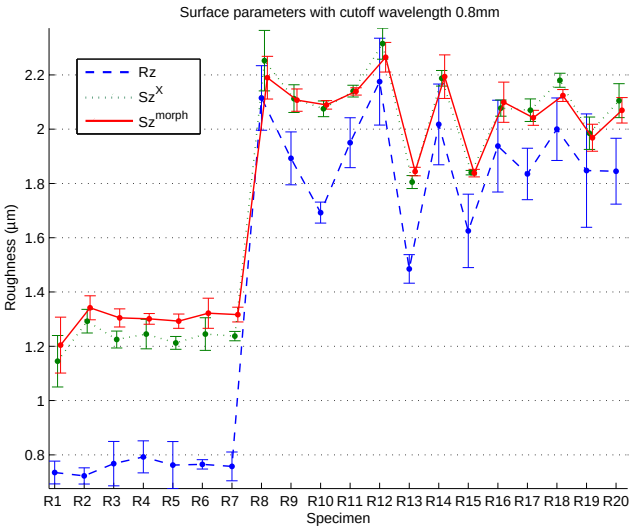

Figure 6.6.: Overview of the roughness parameters obtained for measurements on 20 specimen that underwent grinding (R1-R7) or shot-blasting (R8-R20).

To calculate S_z^{morph}, the radius of the disc-shaped structuring element has to be chosen. Here, for a cutoff wavelength l_r=0.8mm, a radius $r = 10\mu m$ yielded results that best matched the tactile R_z-values.

6.3. Results and Discussion

The results of all calculations are shown in figure 6.6. The horizontal axis distinguishes the specimen $R_1, \ldots, R_{20}$. On the vertical axis, the corresponding roughness values are plotted. The lines show the mean of roughness parameters for the four regions on a specimen and the error bars indicate their standard deviation.

The excellent correlation between the S_z^X values obtained from the Metropro software and the morphological S_z^{morph} is immediately obvious from

figure 6.6. On the data sets examined, both methods yield similar mean values and standard deviations. This finding suggests that S_z^{morph} and S_{vs} are adequate for 3D data from optical measurement systems such as white light interferometry.

If 3D parameters are compared to their 2D counterpart, one notices that they have, in general, a smaller deviation. In figure 6.7, R_z is plotted against S_z^{morph}; each point in the plane corresponds to a tactile R_z– S_z^{morph} pair. Each ellipse represents one specimen, where the orientation and size of the ellipse reflect the spread of the four single measurements. The smaller deviation of the S_z^{morph} values is due to the fact that the S_z^{morph} calculation is based on much more data than is used in tactile methods. Accordingly, outliers have a smaller influence on the calculated parameters.

Fig. 6.6 also shows a systematic difference between R_z and S_z^{morph}. For a better understanding of the correlation between R_z and S_z^{morph}, a straight line (dashed line, fig. 6.7) has been fitted through the R_z-S_z^{morph}-pairs using total least squares [27]. This line shows a small but significant deviation from the straight line through the origin with slope 1 (dotted line). This finding can be explained by outliers found in data acquired with optical measurement instruments [95]. As S_z^{morph} is an extreme value statistic, these outliers cause the trend to values higher than those expected from the tactile R_z-measurements.

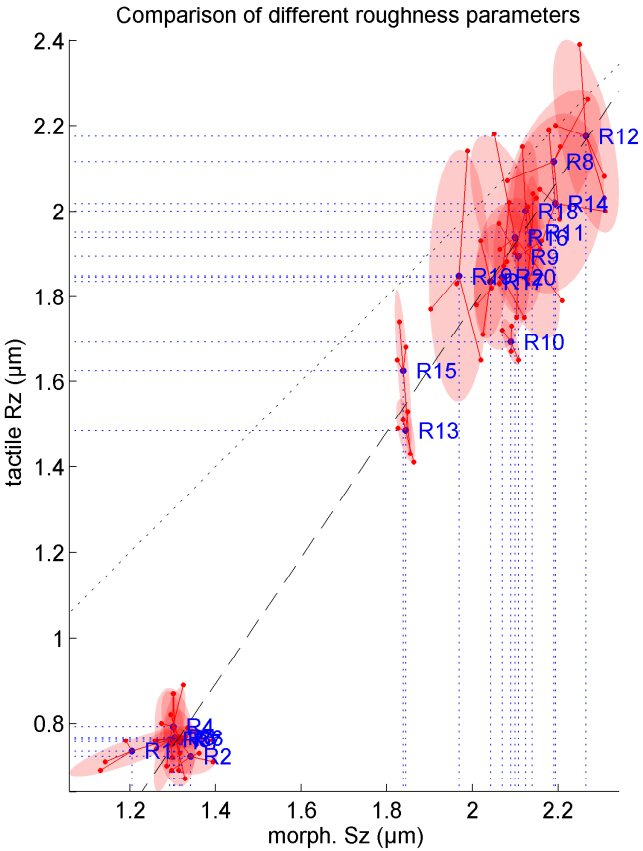

Figure 6.7.: Relation between different parameters from tactile and optical measurements.

7. Conclusions and Outlook

In this thesis, a novel method for the evaluation of measurement data of technical surfaces based on Minkowski functionals has been proposed.

Similar level set techniques, especially the Abbott-Firestone-curve, have been successfully applied in practice before. The Minkowski functionals approach extends these heuristic methods in a systematic and theoretically well-founded way.

The proposed method is capable of describing a wide range of phenomena observable on rotation-invariant surfaces. First, this conclusion can be drawn from Hadwiger's theorem, which states that the Minkowski functionals offer a complete set of descriptors for the level set. Second, it has been shown that the major part of the established three-dimensional surface parameters could also be derived from the Minkowski functionals. In combination with filter techniques, Minkowski functionals can catch the whole information content of homogeneous surfaces up to rotation.

Minkowski functionals become especially interesting when they can be linked to a surface model: Comparing the Minkowski functionals estimated from data with a model's Minkowski functionals can reveal even slight deviations of the real surface from the model. Moreover, if a manufacturing process can be modeled, the process parameters can be automatically determined such that the resulting Minkowski functionals match given values. This will be of great importance when it comes to the design of surfaces with specific properties.

The next step towards a practical application of the Minkowski functionals will be the experimental validation of a correspondence between the Minkowski functionals' values and functional properties of a surface. This will offer the possibility to directly design a surface with the desired functionality; to this day, this has been possible only in a very limited way.

Another application will be manufacturing process control: Starting from a set of surfaces which are known to agree with the specifications, their characterizing functions can be learned by the computer. Comparing a new part's characterizing functions to the former, it can be easily determined if the part deviates significantly from the flawless parts and the reason for the deviation can be figured out. The fast algorithm for the calculation of the Minkowski functionals developed in this thesis even allows for an inline application in manufacturing.

A. Appendix

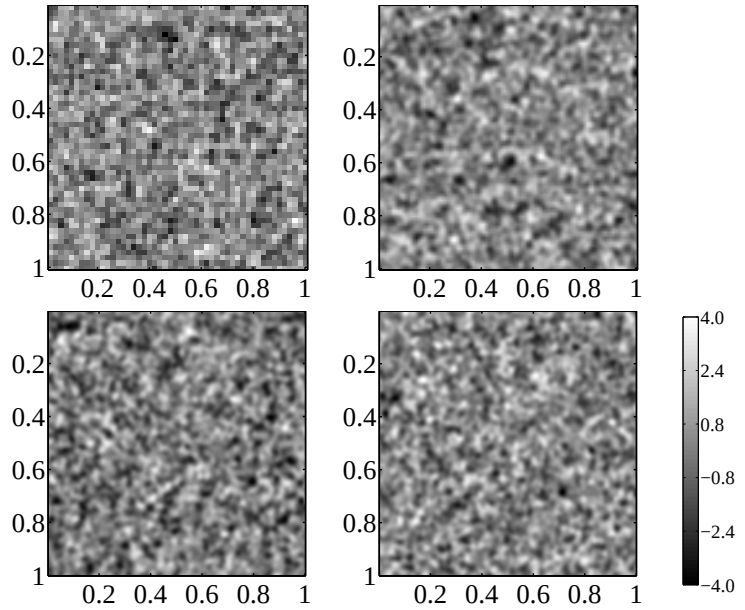

Figure A.1.: Four realizations of the same GRF on a 1×1 window sampled on $n \times n$-lattices with $n = 50, 100, 250, 500$.

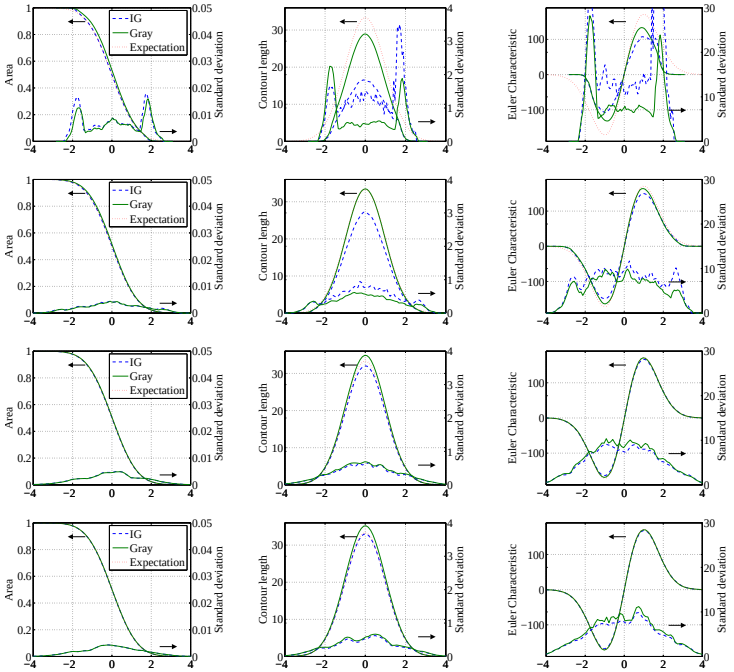

Figure A.2.: Summarized Minkowski functionals and their standard deviations for the GRF used in figure A.1 for 50 realizations each. The rows correspond to the resolutions $n = 50, 100, 250, 500$.

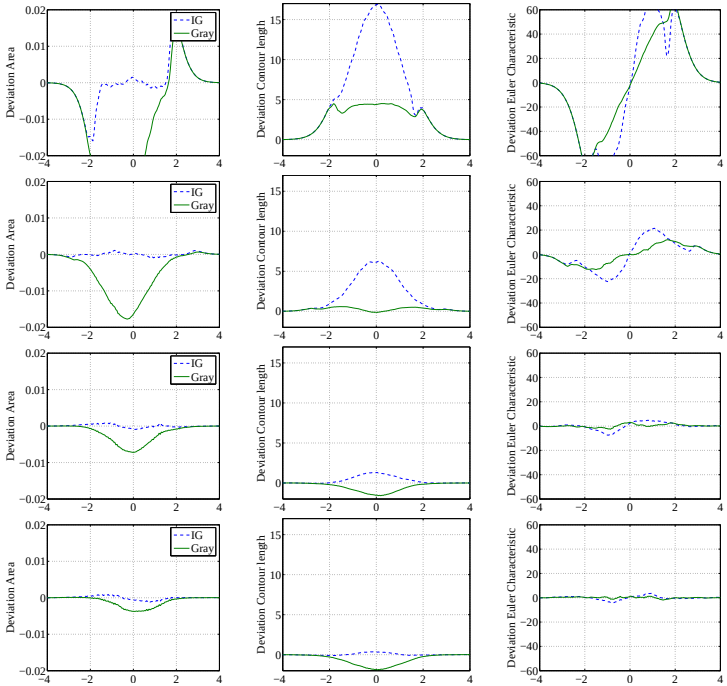

Figure A.3.: Deviations between the mean of the Minkowski functionals estimated from simulations and the expected Minkowski functionals.

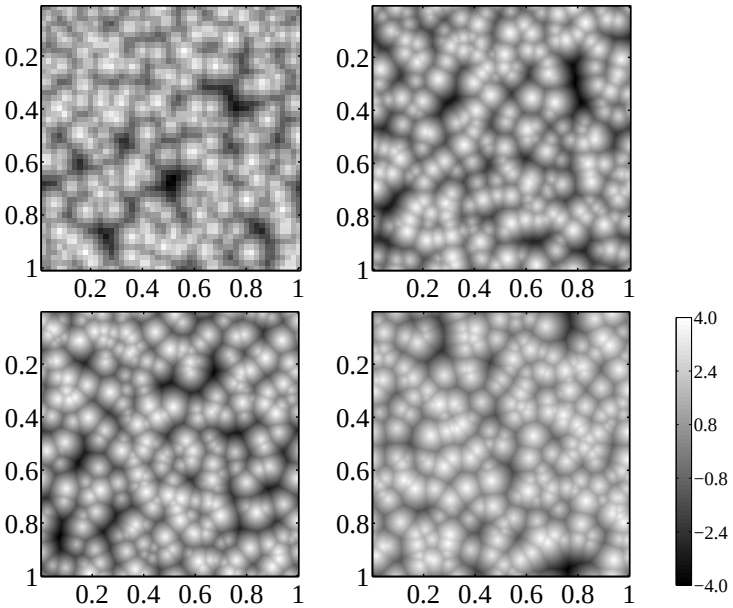

Figure A.4.: Four realizations of the same Boolean grain model on a 1×1 window sampled on $n \times n$-lattices with $n = 50, 100, 250, 500$.

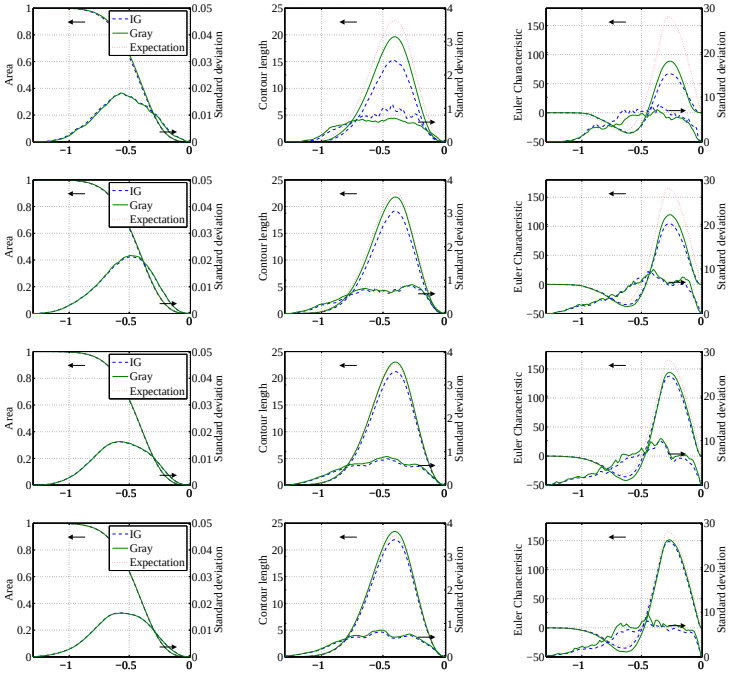

Figure A.5.: Summarized Minkowski functionals and their standard deviations for the Boolean grain model used in figure A.4 for 50 realizations each. The rows correspond to the resolutions $n = 50, 100, 250, 500$.

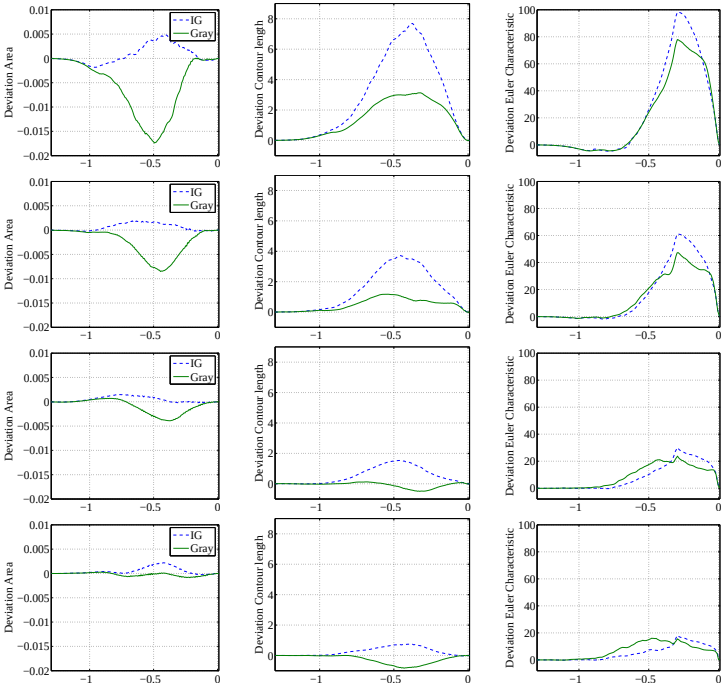

Figure A.6.: Deviations between the mean of the Minkowski functionals estimated from simulations and the expected Minkowski functionals.

Bibliography

[1] E. J. Abbott and F. A. Firestone, *Specifying surface quality: a method based on accurate measurement and comparison*, Mechanical Engineering, 55 (1933), pp. 569–572.

[2] R. J. Adler, *The Geometry of Random Fields*, John Wiley & Sons, 1981. Wiley Series in Probability and Mathematical Statistics.

[3] R. J. Adler and D. Firman, *A non-Gaussian model for random surfaces*, Physical Transactions of the Royal Society of London. Series A, Mathematical and Physical Sciences, 303 (1981), pp. 433–462.

[4] F. Barré and J. Lopez, *Watershed lines and catchment basins: A new 3D-motif method*, International Journal of Machine Tools and Manufacture, 40 (2000), pp. 1171–1184.

[5] ———, *On a 3D extension of the MOTIF method (ISO 12085)*, International Journal of Machine Tools and Manufacture, 41 (2001), pp. 1873–1880.

[6] J. Becker, G. Grün, R. Seemann, H. Mantz, K. Jacobs, K. R. Mecke, and R. Blossey, *Complex dewetting scenarios captured by thin-film models*, Nature Materials, 2 (2003).

[7] M. Beil, H. Braxmeier, F. Fleischer, V. Schmidt, and P. Walther, *Quantitative analysis of keratin filament networks in scanning electron microscopy images of cancer cells*, Journal of Microscopy, 220 (2005), pp. 84–95.

[8] F. Benati, F. Sacerdotti, B. J. Griffiths, C. Butler, J. M. Karila, M. Vermeulen, H. Holtkamp, and S. Gatti, *Correlation between surface topography and lubricant migration in steel sheets for the autobody manufacturing process*, Measurement Science and Technology, 13 (2002), pp. 785–791.

[9] L. Blunt and X. Jiang, *Advanced Techniques for Assessment Surface Topography - Development of a Basis for the 3D Surface Texture Standards SURFSTAND*, Kogan Page Science, London, 2003.

[10] H. F. Boehm, T. M. Link, R. A. Monetti, D. Mueller, E. J. Rummeny, G. Morfill, and C. W. Raeth, *Application of the Minkowski functionals in 3D to high resolution MR images of trabecular bone: prediction of the biomechanical strength by non-linear topological measures*, Proceedings of the SPIE: Medical Imaging: Image Processing, 5370 (2004), pp. 215–224.

[11] J. Boulanger, *The motifs method: An interesting complement to ISO parameters for some functional problems*, International Journal of Machine Tools and Manufacture, 32 (1992), pp. 203–209.

[12] C. Bouman and K. Sauer, *A generalized Gaussian image model for edge-preserving map estimation*, IEEE Transactions on Image Processing, 2 (1993), pp. 296–310.

[13] S. Brinkmann, H. Bodschwinna, and H.-W. Lemke, *Accessing roughness in three dimensions using Gaussian regression filtering*, International Journal of Machine Tools and Manufacture, 41 (2001), pp. 2153–2161.

[14] I. N. Bronstein and K. A. Semendjajew, *Taschenbuch der Mathematik*, Verlag Harri Deutsch AG, Thun, 2000.

[15] C. Brown and S. Siegmann, *Fundamental scales of adhesion and area-scale fractal analysis*, International Journal of Machine Tools and Manufacture, 41 (2001), pp. 1927–1933.

[16] C.-C. A. Chen, W.-C. Liu, and N. A. Duffie, *A surface topography model for automated surface finishing*, International Journal of Machine Tools and Manufacture, 38 (1998), pp. 543–550.

[17] S. Davies and P. Hall, *Fractal analysis of surface roughness by using spatial data*, J. R. Statist. Soc. B, 61 (1999), pp. 3–37.

[18] M. H. de Groot, *Probability and Statistics*, Addison Wesley, 3rd ed., 2001.

[19] M. Dietzsch, M. Gerlach, and S. Gröger, *Back to the envelope system with morphological operations for the evaluation of surfaces*, in Proceedings of the 10th International Conference on Metrology and Properties of Engineering Surfaces, T. Thomas, B. G. Rosen, and H. Zahouani, eds., Saint-Etienne, France, 2005, pp. 143–151.

[20] R. O. Duda and P. E. Hart, *Pattern classification and scene analysis*, John Wiley and Sons, New York, 1973.

[21] C. J. Evans and J. B. Bryan, *Structured, textured or engineered surfaces*, Annals of the CIRP, 48 (1999). Keynote Paper.

[22] W. Feller, *An introduction to probability theory and its applications*, John Wiley, New York, 1971.

[23] S. Gray, *Local properties of binary images in two dimensions*, IEEE Transactions on Computers, 20 (1971), pp. 551–561.

[24] J. A. Greenwood and J. B. P. Williamson, *Contact of nominally flat surfaces*, Proceedings of the Royal Society London, Series A, 295 (1966), pp. 300–319.

[25] H. Hadwiger, *Vorlesungen über Inhalt, Oberfläche und Isoperimetrie*, Springer, 1957.

[26] R. Haralick, K. Shanmugam, and I. Dinstein, *Textural features for image classification*, SMC, 3 (1973), pp. 610–621.

[27] S. V. Huffel and J. Vandewalle, *The Total Least Squares Problem: Computational Aspects and Analysis*, SIAM, Philadelphia, 1991.

[28] D. Hug, G. Last, and W. Weil, *Polynomial parallel volume, convexity and contact distributions of random sets*, Probability Theory and Related, (2005). To appear.

[29] ISO TC 213 Workgroup 16, *Geometrical Product Specifications (GPS) - Surface Texture: Areal - Part 2: Terms, Definitions and Surface Texture Parameters*, 2005. Standard proposal N756.

[30] *ISO16610. Geometrical product specifications (GPS) – Filtration – Part 1: Overview and Basic Concepts*, 2004.

[31] *ISO 4287:1997. Geometrical Product Specifications (GPS) – Surface Texture: Profile method*, 1997.

[32] B. Jähne, ed., *Handbook of Computer Vision and Applications*, vol. 2, Academic Press, San Diego, 1999.

[33] X. Jiang and L. Blunt, *Third generation wavelet for the extraction of morphological features from micro and nano scalar surfaces*, Wear, 257 (2004), pp. 1235–1240.

[34] B. Josso, D. R. Burton, and M. J. Lalor, *Frequency normalised wavelet transform for surface roughness analysis and characterisation*, Wear, 252 (2002), pp. 491–500.

[35] S. Klenk, J. Mayer, V. Schmidt, and E. Spodarev, *Algorithms for the computation of minkowski functionals of deterministic and random polyconvex sets*. Preprint, 2005.

[36] K.-H. Kopplin, *Kennwerte zur Charakterisierung von Feinblechoberflächen*. Private communication, 2003.

[37] S.-H. Lee, H. Zahouani, R. Caterini, and T. Mathia, *Morphological characterisation of engineered surfaces by wavelet transform*, International Journal of Machine Tools and Manufacture, 38 (1998), pp. 581–589.

[38] S. Z. Li, *Markov random field modeling in image analysis*, Springer-Verlag New York, Inc., Secaucus, NJ, 2001.

[39] J. S. Lim, *Two-dimensional signal and image processing*, Prentice-Hall, Inc., Upper Saddle River, NJ, 1990.

[40] T. Lindeberg, *Scale-Space Theory In Computer Vision*, Kluwer Academic Publishers, Dordrecht, 1994.

[41] S. N. Magonov and M.-H. Whangbo, *Surface analysis with STM and AFM*, VCH, Weinheim, 1996.

[42] M. C. Malburg, *Surface profile analysis for conformable interfaces*, Transactions of the ASME, 125 (2003), pp. 624–627.

[43] S. Mallat, *A Wavelet Tour of Signal Processing*, Academic Press, New York, 1998.

[44] G. Matheron, *Random Sets and Integral Geometry*, John Wiley and Sons, New York, 1975.

[45] J. McCool, *Characterization of surface anisotropy*, Wear, 49 (1978), pp. 19–31.

[46] K. Mecke and C. H. Arns, *Fluids in porous media: a morphometric approach*, J. Phys.: Condens. Matter, 17 (2005), pp. 503–534.

[47] K. R. Mecke, *Additivity, Convexity, and Beyond: Applications of Minkowski Functionals in Statistical Physics*, LNP Vol. 554: Statistical Physics and Spatial Statistics. The Art of Analyzing and Modeling Spatial Structures and Pattern Formation, 554 (2000), pp. 111–183.

[48] K. R. Mecke, T. Buchert, and H. Wagner, *Robust morphological measures for large-scale structure in the universe*, Astronomy and Astrophysics, 288 (1994), pp. 697–704.

[49] K. R. Mecke and D. Stoyan, eds., *Statistical Physics and Spatial Statistics*, vol. 554 of Lecture Notes in physics, Springer, Berlin, 2000, ch. Statistical Analysis of Large-Scale Structure in the Universe, pp. 36–71.

[50] K. R. Mecke and H. Wagner, *Euler characteristic and related measures for random geometric sets*, journal of Statistical Physics, 64 (1991), pp. 843 – 850.

[51] F. Meyer and P. Maragos, *Morphological scale-space representation with levelings*, in Scale Space, 1999, pp. 187–198.

[52] J. Møller and R. Waagepetersen, *Statistical Inference and Simulation for Spatial Point Processes*, Chapman and Hall, Boca Raton, 2003.

[53] H. Moalic, J. A. Fitzpatrick, and A. A. Torrance, *A spectral approach to the analysis of rough surfaces*, Transactions of the ASME, Journal of Tribology, 111 (1989), pp. 359–363.

[54] I. Molchanov, *Theory of Random Sets*, Springer, London, 2005.

[55] I. S. Molchanov, *Statistics of the Boolean model: From the estimation of means to the estimation of distributions*, Advances in Applied Probability, 27 (1995), pp. 63–86.

[56] S. Mukhopadhyay and B. Chanda, *Multiscale morphological segmentation of gray-scale images*, IEEE Trans. Image Proc., 12 (2003), pp. 533–549.

[57] B. Muralikrishnan and J. Raja, *Topography characterization of engineering surfaces using mathematical morphology*, Journal of Manufacturing Science and Engineering, 127 (2005), pp. 193–197.

[58] N. Myshkin., A. Grigoriev, S. Chizhik, K. Choi, and M. Petrokovets, *Surface roughness and texture analysis in microscale*, Wear, 254 (2003), pp. 1001–1009.

[59] W. Nagel, J. Ohser, and K. Pischang, *An integral-geometric approach for the euler-poincaré characteristic of spatial images*, Journal of Microscopy, 189 (2000), pp. 54–62.

[60] P. R. Nayak, *Random process model of rough surfaces in plastic contact*, Wear, 26 (1973), pp. 305–333.

[61] D. Novikov, H. A. Feldman, and S. F. Shandarin, *Minkowski functionals and cluster analysis for CMB maps*, International Journal of Modern Physics D, 8 (1999), p. 291.

[62] J. Ohser and F. Mücklich, *Statistical Analysis of Microstructures in Materials Science*, John Wiley & Sons Ltd., New York, 2000.

[63] J. Ohser, B. Steinbach, and C. Lang, *Efficient texture analysis of binary images*, Journal of Microscopy, 192 (1998), pp. 20–28.

[64] M. Pfestorf, U. Engel, and M.Geiger, *3D-surface parameters and their application on deterministic textured metal sheets*, International Journal of Machine Tools and Manufacture, 38 (1998), pp. 607–614.

[65] U. Popp, T. Neudecker, U. Engel, and M. Geiger, *Surface characterization with regard to the tribological behaviour of sheet metal in forming process*, in Proceedings of the SheMet '99, M. Geiger, H. Kals, B. Shirvani, and U. P. Singh, eds., 1999.

[66] S. Rana and J. Morley, *Surface networks*, working paper, Centre for Advanced Spatial Analysis, University College London, 2002.

[67] B. D. Ripley, 1999. Discussion in "Fractal Analysis of Surface Roughness by Using Spatial Data" by Davies and Hall.

[68] F. Sacerdotti, F. Benati, C. Butler, and B. Griffiths, *Closed regions: a proposal for spacing parameters for areal surface measurements*, Measurement Science and Technology, 13 (2002), pp. 556–564.

[69] L. Santaló, *Integral Geometry and Geometric Probability*, Addison-Wesley, Reading, Mass., 1976.

[70] R. S. Sayles and T. R. Thomas, *Surface topography as a non-stationary random process*, Nature, 271 (1978), pp. 431–434.

[71] M. Schlather, *Introduction to positive definite functions and to unconditional simulation of random fields*, Tech. Report ST-99-10, Department of Mathematics and Statistics, Lancaster University, UK, 1999.

[72] J. Schmähling and F. A. Hamprecht, *Minkowski functionals in the analysis of technical surface microstructure*, Submitted to Wear, (2006).

[73] J. Schmähling, F. A. Hamprecht, and D. M. P. Hoffmann, *A three-dimensional measure of surface roughness based on mathematical morphology*, To be published in International Journal of Machine Tools and Manufacture, (2006).

[74] J. Schmalzing, *On Statistics and Dynamics of Cosmic Structure*, PhD thesis, Ludwig-Maximilians-Universität München, 1999.

[75] V. Schmidt and E. Spodarev, *Joint estimators for the specific intrinsic volumes of stationary random sets*, Stochastic Processes and their Applications, 115 (2005), pp. 959–981.

[76] M. Schmitt, *Mathematical morphology for shape description*, Journal de Physique IV, 12 (2002), pp. 87–116.

[77] R. Schneider and W. Weil, *Integralgeometrie*, B. G. Teubner, Stuttgart, 1992.

[78] P. J. Scott, *An algorithm to extract critical points from lattice height data*, International Journal of Machine Tools and Manufacture, 41 (2001), pp. 1889–1897.

[79] ———, *Pattern analysis and metrology: The extraction of stable features from observable measurements*, Proceedings of the Royal Society London, Series A, 460 (2004), pp. 2845–2864.

[80] L. A. Seneca, *L. Annaei Senecae epistularum moralium ad Lucilium liber XIII, ep. LXXXVIII.*

[81] J. Serra, *Image Analysis and Mathematical Morphology*, Academic Press, London, 1982.

[82] J. Staeves, *Beurteilung der Topografie von Blechen im Hinblick auf die Reibung bei der Umformung*, PhD thesis, TU Darmstadt, 1998.

[83] M. L. Stein, *Interpolation of Spatial Data - Some Theory for Kriging*, Springer, 1999.

[84] K. J. Stout and L. Blunt, eds., *Methods for the development of surface parameters in three dimensions*, Kogan Page Science, London, 2000.

[85] ———, *A contribution to the debate on surface classifications - random, systematic, unstructured, structured and engineered*, International Journal of Machine Tools and Manufacture, 41 (2001), pp. 2039–2044.

[86] D. Stoyan, W. S. Kendall, and J. Mecke, *Stochastic Geometry and its Applications*, Wiley, Chichester, second ed., 1995.

[87] A. Suh, A. A. Polycarpou, and T. F. Conry, *Detailed surface roughness characterization of engineering surfaces undergoing tribological testing leading to scuffing*, Wear, 255 (2003), pp. 556–568.

[88] T. R. Thomas, *Rough Surfaces*, Imperial College Press, London, 2nd ed., 1999.

[89] H. Tomita, *Statistics and geometry of random interface systems*, in Formation, Dynamics and Statistics of Patterns, K. Kawasaki, M. Suzuki, and A. Onuki, eds., vol. 1, World Scientific, 1990, pp. 113–156.

[90] Topocrom GmbH, 2006. www.topocrom.com.

[91] A. Tscheschel, D. Stoyan, and R. Hilfer, *Erosion-dilation analysis for experimental and synthetic microstructures of sedimentary rock*, Physica A, 284 (2000), p. 46.

[92] M. Tuceryan and A. K. Jain, *Texture analysis*, in The Handbook of Pattern Recognition and Computer Vision (2nd Edition), C. H. Chen, L. F. Pau, and P. S. P. Wang, eds., World Scientific Publishing Co., 1998, pp. 207–248.

[93] H. von Weingraber, *Suitability of the envelope line as a reference standard for measuring roughness*, Microtecnic, 11 (1957), pp. 6–17.

[94] M. Wächter, *Markov-Analysen unebener Oberflächen*, PhD thesis, Carl von Ossietzky-Universität Oldenburg, 2004.

[95] A. Weidner, J. Seewig, and E. Reithmeier, *Structure oriented 3D roughness evaluation with optical profilers*, in Proceedings of the 10th International Conference on Metrology and Properties of Engineering Surfaces, T.Thomas, B. Rosen, and H. Zahouani, eds., Saint-Etienne, France, 2005, pp. 49–58.

[96] W. Weil, *The estimation of mean shape and mean particle number in overlapping particle systems in the plane*, Advances in Applied Probability, 27 (1995), pp. 102–119.

[97] J. S. Weszka and A. Rosenfeld, *An application of texture analysis to materials inspection*, Pattern Recognition, 8 (1976), pp. 195–199.

[98] D. J. Whitehouse, *Surface metrology*, Measurement Science and Technology, 8 (1997), pp. 955–972.

[99] ———, *Fractal or fiction*, Wear, 249 (2001), pp. 345–353.

[100] D. J. Whitehouse and J. F. Archard, *The Properties of Random Surfaces of Significance in their Contact*, Royal Society of London Proceedings Series A, 316 (1970), pp. 97–121.

[101] A. Wihlborg and L. Gunnarsson, *A frictional study of uncoated EBT steel sheets in a bending under tension friction test*, Wear, 237 (2000), pp. 129–136.

[102] S. Winitzki and A. Kosowsky, *Minkowski functional description of microwave background gaussianity*, New Astronomy Reviews, 3 (1998), p. 75.

[103] G. Winkler, *Image analysis, random fields and dynamic Monte-Carlo methods*, Springer-Verlag, Berlin, 1995.

[104] G. W. Wolf, *A Fortran subroutine for cartographic generalization*, Computers and Geoscience, 17 (1991), pp. 1359–1381.

[105] A. Wood and G. Chan, *Simulation of stationary gaussian processes in* $[0, 1]^d$, Journal of Computational and Graphical Statistics, 3 (1994), pp. 409–432.

[106] K. Worsley, *Local maxima and the expected Euler characteristic of excursion sets of χ^2, F and t-fields*, Advances in Applied Probability, 13 (1994).

[107] H. Zahouani, *Spectral and 3D motifs identification of anisotropic topographical components. analysis and filtering of anisotropic patterns by morphological rose approach*, International Journal of Machine Tools and Manufacture, 38 (1998), pp. 615–623.

[108] Zygo Corporation, *Metropro Reference Guide*, Middlefield, 2004.